Changes in Cyclone Characteristics over the North Atlantic in the Norwegian Earth System Model

Sofie Mykkeltveit Tunes

Thesis submitted for the degree of
Master of science in Meteorology and Oceanography
60 Credits

Department of Geosciences
Faculty of mathematics and natural sciences

UNIVERSITY OF OSLO

November 29, 2021

Changes in Cyclone Characteristics over the North Atlantic in the Norwegian Earth System Model

This work is published digitally through DUO – Digitale Utgivelser ved UiO
`http://www.duo.uio.no/`

Printed: Reprosentralen, University of Oslo

Abstract

Motivated by the low confidence in regional storm track changes, this study investigates the winter North Atlantic extra-tropical storm track for the NorESM2-MM model in phase 6 of the Coupled Model Intercomparison Project. The state of the storm track from 1980 to 2014 is compared to that in ERA-Interim using a Lagrangian objective cyclone tracking algorithm, applied to the mean sea-level pressure. Changes in cyclone characteristics are examined by comparing the abrupt-4xCO2 and SSP5-8.5 scenario simulations to control runs.

A good agreement is found between the NorESM2 and ERA-Interim. The uncertainties that still persist in the model are suggested to be a result of a too coarse horizontal resolution, and the inability of the model to resolve diabatic processes.

The results in this study differ from the general consensus of a poleward shift of the genesis latitude. A tripole structure is found with more genesis in mid-latitudes (40-60°N) and less to the north and south. This is found to be a result of the negative meridional temperature gradient anomaly in mid-latitudes which creates a locally enhanced baroclinicity due to sea-ice and SST processes. An overall reduction in the number of storms of about 10 % is found in both scenarios. The reduction is linked to the decrease in the low-level meridional temperature gradient, which reduces the available potential energy for the cyclones. In addition, a more efficient poleward heat transport is suggested due to increased water vapor in a future climate, so less storms could perform the same heat transport.

The storms translate farther, both polewards and eastwards. This is linked to the strengthening of the upper jet and the increased cyclone-related precipitation. No change was found for the cyclones lifetimes, which indicate that they also travel faster. The number of weak storms are expected to increase. Even if more latent heat are expected in the future, the overall effect of moistening is to make the storms weaker by improving the efficiency of poleward heat transport and reducing the baroclinicity. Thus, we can get more precipitation, despite no increase in the intensity.

Acknowledgements

First, I would like to thank my main supervisor, Joseph H. LaCasce. Thank you for making this thesis possible, and for your excellent guidance. I would also like to thank my co-supervisor, Lise Seland Graff, for guiding me through all of the technical questions, and for all your great advice. Thank you both for being patient with me, making it possible to finish this thesis while playing soccer at the top level.

I would also like to thank Thomas Spengler for bringing new and interesting ideas for the analysis in this thesis.

Thank you to Geo IT and especially Sunniva Indrehus for helping me compile the tracking algorithm, and making it run smoothly.

To my fellow students, thanks for all the amusing conversations and great support.

Last but not least, thank you to my family and friends, for being there for me and motivating me throughout this process.

Oslo, November 2021
Sofie Mykkeltveit Tunes

Contents

List of Figures

List of Tables

1 Introduction

1.1 Motivation and background

Extra-tropical cyclones (from now on referred to as cyclones or storms) dominate the day-to-day variability of weather in the mid-latitudes. Cyclones can bring wind, temperature and precipitation extremes to populated areas, such as Europe (Catto et al., 2011). Severe weather events like these can have large socioeconomic impact, which makes cyclones subject to much attention (Holton, 2004). One example of such impact was the New Year's Day storm that swept over the northwestern coast of Norway 1. January 1992 (Figure 1.1). With wind speeds up to 45 m s^{-1}, it reached hurricane levels. The cyclone is thought of as the most devastating storm in Norwegian history, with damage costs estimated to more than a billion (NOK) (Harstveit, 2019). As the climate changes in response to increased CO_2 levels, the societal and economical impact of the cyclones could also change (Catto et al., 2011). A systematic change in a cyclone's characteristics, such as position, frequency or intensity will consequently have a large influence on the local climate (Bengtsson and Hodges, 2006).

Figure 1.1: New Year's Day storm, Molde marina January 1st 1992. Photo by Kjell Herskedal, NTB.

Not only do the cyclones influence the weather, they also impact the global climate through transport of energy and momentum (Shaw et al., 2016). Cyclones are observed to form, travel and decay preferentially within confined regions known as storm tracks. This study will focus on the North Atlantic (NA) storm track, which begins at the east coast of the United States and follows a north-eastward direction towards Europe (Brayshaw et al., 2009). The region is well suited for cyclone formation due to baroclinic instability. This dynamical mechanism arises from the existence of a meridional temperature gradient and planetary rotation. The vertical shear in the jet stream is linked to the meridional temperature gradient through the thermal wind balance. Hence, horizontal and vertical temperature gradients are key variables in determining the influence of cyclones. In this study the focus will be on the boreal winter, December, January and February (DJF), when the NA storm track reaches maximum intensity due to strong surface baroclinicity (Shaw et al., 2016).

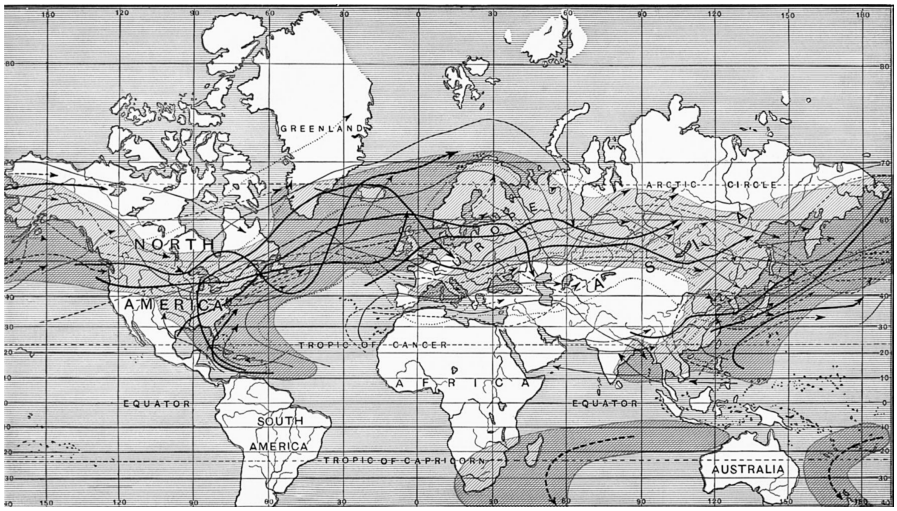

Figure 1.2: Storm frequency distribution as viewed in the mid-nineteenth century. The stipling denotes areas of high storm frequency, while the arrows indicate individual storm trajectories. Figure by Hinman (1888).

The characteristics of storm tracks have been a topic of interest for more than a century. The synoptic classification of storm tracks dates at least to the mid-nineteenth century (Schultz et al., 2019). Russell Hinman produced a figure in 1988 (Figure 1.2), showing the observed storm frequency and storm trajectories. Many of the features seen then are remarkably familiar to the modern synoptic picture of cyclone distribution. Even without a clear distinction between extra-tropical and tropical cyclones, the traditional NA and North Pacific (NP) storm tracks stand out (Chang et al., 2002). When the computers arrived, more advanced methods for storm track identification and analysis developed. To identify a cyclone's position, several variables can be used, such as relative vorticity, eddy kinetic energy (EKE), geopotential height and

mean sea level pressure (MSLP). In addition to the choice of variable for identification, there are two common frameworks for analysing storm tracks, namely the Eulerian- and Lagrangian approaches (Walker et al., 2020). More information on these approaches and the specific methods are found under Section 2.1. The development in this field has lead to a broad selection of studies attempting to answer one of the major questions, namely, "how will the NA storm track respond to anthropogenic climate change?".

Overall, the Intergovernmental Panel on Climate Change (IPCC) found low confidence in the magnitude of regional storm track changes in the Fifth Assessment Report (AR5). Uncertainty remains in projecting changes for the Northern Hemisphere (NH) storm tracks, especially for the NA basin (Stocker et al.). Brayshaw et al. (2009) note that future projections for this region are especially difficult, due to the complex range of forcings (land–sea contrast, orography, sea-surface temperatures (SSTs), etc.) which together produce the structure of this storm track. AR5 shows that the response of the NA storm track is unlikely to be a simple poleward shift, and that the precipitation linked to cyclones are projected to increase (Stocker et al.). Nevertheless, previous studies with aquaplanet simulations and/or runs with idealized forcing agree on a poleward shift in storm tracks (Graff and LaCasce, 2012; Lu et al., 2010; Mbengue and Schneider, 2013; Shaw and Voigt, 2016). However, the magnitude of the response varies based on the chosen simulation and the area of interest. Since AR5, the storm track projections have been further examined, and the previous estimations are mostly confirmed. The Sixth Assessment Report (AR6) still finds low confidence in projected changes for the NA storm track (IPCC, a). As stated in AR5, it is unlikely that the NA storm track will display any discernible changes in its position. When it comes to the cyclone numbers, models from the Coupled Model Intercomparison Project phase 6 (CMIP6) show an overall low agreement on how the cyclone density will change in NA. However, there is medium confidence that the intense cyclones in NH will decrease in frequency. Regardless of how the intensity will change, there is high confidence that the number of cyclones associated with extreme precipitation will increase due to the increased atmospheric water vapor (Lee et al.). Further projections for this storm track are found under Section 2.3.

The low confidence level in cyclone projections are partly due to complex processes. The future characteristics of storm tracks depend on processes that alter the temperature gradients. For example, as climate warms, more precipitation could be expected due to the Clausius-Clapeyron relation, which states that a warmer atmosphere can hold more moisture (Shaw et al., 2016). Furthermore, this could lead to an increase in the intensity of cyclones due to more latent heat release (Bengtsson and Hodges, 2006). However, the atmosphere does not warm uniformly with climate change. The warming is amplified at low levels in the Arctic, by so-called Arctic amplification, and at upper levels in the tropics. The former effect acts to reduce the low-level Equator-to-pole temperature gradient, while the latter increases the upper-level temperature

gradient (Shaw et al., 2016). Aside from these effects, storm track changes can be linked to the subtropical jet, extra-tropical SSTs, Arctic sea ice loss, the stratospheric polar vortex, large-scale phenomena such as the North Atlantic Oscillation (NAO) etc. (Walker et al., 2020; Douville et al.).

Complex processes and the variety of data sets, tracking methods and definitions of extremes have lead to diverse results, which makes future projections of storm tracks difficult, especially in NA (Walker et al., 2020; Ulbrich et al., 2009; Neu et al., 2013). Overall, progress in this field depends on additional observations and filling the gaps in the model hierarchy. Further studies are necessary to gain a better understanding of the processes, and to reduce uncertainties of the storm track response to climate change (Shaw et al., 2016).

1.2 Description of this study

The NA storm track affects populated areas, and there is still low confidence in the projected changes. Therefore, the two main objectives in this present study are too:

1. *Assess how realistic the Norwegian Earth System Model (NorESM) is at capturing cyclones*
2. *Examine changes in NA cyclone characteristics occurring in climate scenario simulations*

Data from experiments carried out for CMIP6 with the second version of NorESM (NorESM2) will be examined. The experiments used are the historical and pre-industrial control (piControl) runs, and the SSP5-8.5 and abrupt-4xCO2 scenarios (see Section 3.1). The cyclone characteristics are determined using an objective Lagrangian tracking algorithm, applied to the MSLP. The algorithm is called the University of Melbourne Cyclone Detection and Tracking Algorithm (described in Section 4.1) which both identifies and follows the cyclones in time (Murray and Simmonds, 1991a). For the first part, a comparison of the statistic from the historical run with the statistics from a reanalysis called ECMWF Re-Analysis Interim (ERA-Interim) is made, and the extent of the mismatch is assessed (Dee et al., 2011). For the second part, we study how the frequency, position and intensity of cyclones are changing by comparing the historical experiment with the SSP5-8.5 scenario, and the piControl run with the abrupt-4xCO2 scenario. We will further restrict the scope to a monthly evolution from December to February (DJF), and focus on the NA storm track with cyclones that live longer than two days.

This thesis proceeds in seven chapters. An overview of important cyclone theory is given in Chapter 2, the data and methods used are demonstrated in Chapter 3 and Chapter 4, respectively. The results are presented in Chapter 5, followed by a discussion in Chapter 6. Finally, a conclusion and suggestions for future work are given in Chapter 7.

2 | Background theory

This chapter begins with the definitions used for cyclones and storm tracks (2.1), followed by the relevant background theory on where and why cyclones form (2.2). The last section provides a literature study of the projected changes for the NA storm track (2.3).

2.1 Definitions

Extra-tropical cyclones

The IPCC defines extra-tropical cyclones as "any cyclonic-scale storm that is not a tropical cyclone". Usually, this refers to storm systems in middle- or high-latitudes that form in regions of large horizontal temperature gradients. These are also known as extra-tropical lows or extra-tropical storms (IPCC, b).

Cyclones exist due to the baroclinic nature of the mid-latitude atmosphere (see Section 2.2). Another word for the development of synoptic-scale weather disturbances is cyclogenesis (or genesis) (Holton, 2004). Cyclones start of as small perturbations in the mean flow and grow by extracting energy from it. Thus, baroclinic conversion of the available potential energy makes up the main energy source for the cyclones. Cyclogenesis typically starts when perturbations are found in areas of high baroclinicity. These regions are often on the western end of the storm tracks, and are called entrance regions. Such regions are typically found where the land-ocean heat contrasts cause large local meridional temperature gradients (Chang et al., 2002). After cyclogenesis, the cyclones typically travel east along with the jet stream and grow as they are advected downstream (Holton, 2004). Due to landmasses, orography etc. the NA cyclones occur in a region with a southwest-northeast tilt (Brayshaw et al., 2011). The final step is cyclolysis, the process of cyclone decay. The energy is lost to surface friction, wave breaking and barotropic conversion (Martin, 2006; Chang et al., 2002).

Storm tracks

The IPCC loosely defines storm tracks as the main regions where tracks of extra-tropical disturbances occur as sequences of low- and high pressure systems (IPCC, b).

Depending on the approach, different storm track definitions exist. When analysing cyclones one typically distinguish between the Lagrangian and the Eulerian approach. By Lagrangian we mean that we follow the cyclone throughout its life cycle, while in a Eulerian formulation the cyclone is observed as it passes through a fixed location (LaCasce, 2020). Eulerian methods are more straightforward, but they are less selective and do not give out all the information we might want to know about the storm systems (Hoskins and Hodges, 2002; Graff and LaCasce, 2012). The three most common methods for identification and analysis are described in the following.

Feature point identification was an early method, which identifies and counts low pressure centers (often in sea level pressure). This method gives out information on where low pressure centres statistically are found in time and space. In this context, storm tracks are defined as regions with high cyclone count densities (Reitan, 1974; Benestad and Chen, 2006).

Feature point tracking is a more advanced method that builds on feature point identification. This method yields information about the cyclone during its whole life cycle, by computing trajectories of the low-pressure centers. Details on where cyclones are formed, where they travel, how fast they travel, where they decay etc. can be extracted. In this case, storm tracks are defined as areas with high frequency of cyclone trajectories (Murray and Simmonds, 1991a; Sinclair, 1994; Hoskins and Hodges, 2002). In this thesis we use this particular definition.

The bandpass filter method involves bandpass (BP) filtered fields (e.g. geopotential height), to retain fluctuations with time scales corresponding to baroclinic waves. The BP method is less selective than cyclone tracking. However, the easy reproducible method can be carried out at any altitude in the atmosphere, allowing for three-dimensional reconstructions of storm tracks (Chang et al., 2002). The storm tracks are in this case evident as maxima in the BP variance field (Blackmon, 1976; Blackmon et al., 1977). The BP field approach is an Eulerian analysis, based on averaging fields, while cyclone tracking is closer to a Lagrangian one.

2.2 The driving mechanisms

To be able to detect changes in the NA storm track it is essential to understand the mechanisms that drive the cyclones. This section covers the basic aspects of the general atmospheric

circulation and the important mechanism for cyclone formation, namely baroclinic instability.

2.2.1 The general circulation of the atmosphere

The circulation of wind in the atmosphere is driven by the incoming energy from the Sun and the rotation of the Earth. Solar heating is strongly dependent on latitude, with a maximum at the equator and a minima at the poles. This sets up a meridional temperature gradient which is decreasing from the equator towards the poles. To maintain this temperature gradient there has to be an energy transport from the tropics towards the poles. However, the effects of rotation must be taken into account. The Coriolis effect changes the picture of a hemispheric wide thermally direct circulation. When an air parcel moves polewards, the distance between the parcel and the axis of rotation decreases, so for the parcel to conserve its angular momentum it must attain a positive zonal velocity. In the NH the Coriolis force will act to deflect the air parcel to the right. Combining the effect from the Sun and Earths rotation, one can find that as the warm tropical air flows polewards it continues to be deflected to the right. Eventually, the Coriolis force will balance the meridional pressure gradient force yielding geostrophic balance (Equation 2.1), and hence we get a zonal flow at mid-latitudes (Figure 2.1) (Holton, 2004).

$$fu = -\frac{1}{\rho}\frac{\partial p}{\partial y} \tag{2.1}$$

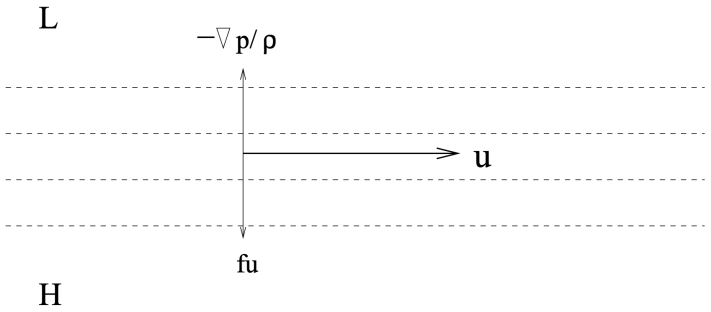

Figure 2.1: Illustration of geostrophic balance in the NH from LaCasce (2020). The Coriolis term (fu) balances the pressure gradient term ($-\frac{1}{\rho}\frac{\partial p}{\partial y}$) as in Equation 2.1, and the flow is parallel to the pressure contours.

Assuming that the atmosphere is in hydrostatic balance, the pressure derivative of the geostrophic balance (Equation 2.1) in pressure coordinates ($u_g = -\frac{1}{f_0}\frac{\partial \Phi}{\partial y}$) can be combined with the hydrostatic balance equation ($\frac{\partial \Phi}{\partial p} = -\frac{RT}{p}$). From this we obtain the thermal wind balance:

$$f\frac{\partial u_g}{\partial p} = \frac{R}{p}\frac{\partial T}{\partial y} \tag{2.2}$$

$$f\frac{\partial v_g}{\partial p} = -\frac{R}{p}\frac{\partial T}{\partial x} \tag{2.3}$$

where u_g is the zonal geostrophic velocity and v_g is the meridional. R is the gas constant of dry air and f is the Coriolis parameter ($f = 2\Omega sin\phi$, where Ω is the angular velocity and ϕ is the latitude). The pressure is denoted by p, and is used as the vertical coordinate. The stronger the meridional temperature gradient ($\frac{\partial T}{\partial y}$), the stronger the vertical shear of the geostrophic zonal wind ($\frac{\partial u_g}{\partial p}$). Due to the thermal wind balance, mid-latitudes are characterized by westerlies, geostrophic zonal winds that increase with height (Holton, 2004). The jet stream refers to the core of fast-flowing winds found at the tropopause level where westerlies reaches maximum strength (Martin, 2006). The westerlies can reach a critical value and become baroclinically unstable, which takes us to the next topic, baroclinic instability (Holton, 2004).

2.2.2 Baroclinic instability

The commonly accepted mechanism responsible for the existence of cyclones is baroclinic instability, and the first models of instability were developed by Charney (1947) and Eady (1949). In a baroclinic fluid the density depends on both temperature and pressure, while in a barotropic fluid the density only depends on the pressure. The geostrophic wind in a baroclinic atmosphere generally has a vertical shear, as seen in the thermal wind equation (Equation 2.2). This is illustrated in Figure 2.2, where the baroclinic fluid have zonal winds which increase with altitude, while for the barotropic fluid the winds do not change with height (Holton, 2004).

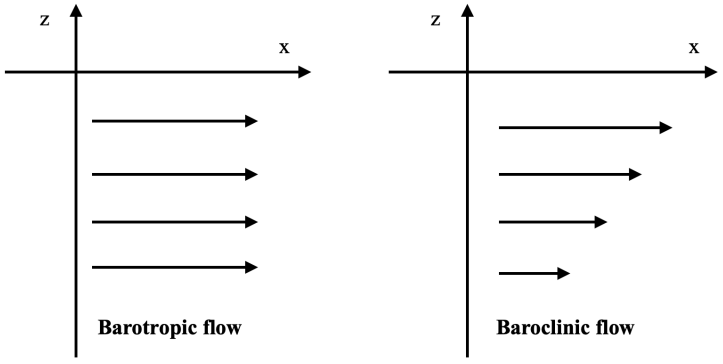

Figure 2.2: Examples vertical wind profiles in a barotropic and a baroclinic fluid.

Baroclinic instability is a characteristic of rotating, stratified fluids. It requires a horizontal temperature gradient and planetary rotation. As discussed in Section 2.2.1 these criteria are met in the mid-latitudes. Baroclinic instability converts potential energy of a fluid into the kinetic energy of perturbations, such as eddies and cyclones (Shaw et al., 2016).

Figure 2.3 shows the basis for baroclinic instability, namely slantwise convection. The temperature decreases to the north, and increases going upwards. The parcel A is therefore colder and heavier than parcel C. If one were to exchange parcel A and C one would increase the potential energy and the air is thus stably stratified. The parcel B is above A and heavier, so exchanging these would release potential energy. This release is referred to as slantwise convection and acts to reduce both the vertical shear and the meridional temperature gradient (LaCasce, 2020). Slantwise convection explains how storms feed on the energy of the mean flow. In other words, cyclones originate from perturbations of the baroclinically unstable current and the perturbations then amplifies by slantwise convection (Holton, 2004).

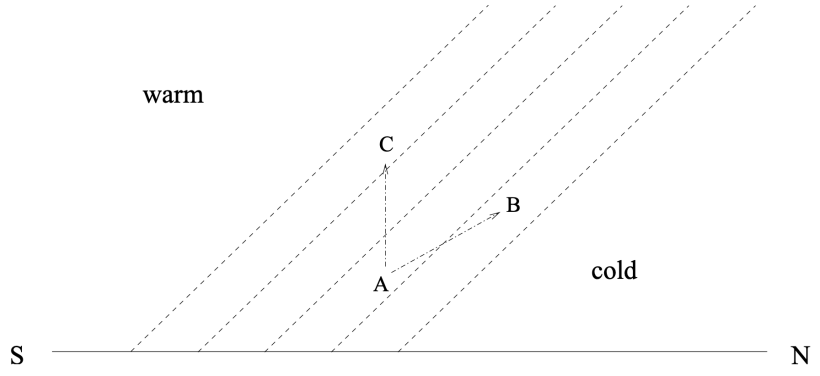

Figure 2.3: Illustration of slantwise convection from Pedlosky (1987) and LaCasce (2020). The stippled lines are slanted isotherms accompanied by a thermal wind shear. The letters A, B and C indicate parcel positions and the arrows indicate two possible ways of interchanging them.

The Eady model

The Eady model (1949) is arguably the simplest model of baroclinic instability. The composition of the Eady model is shown in Figure 2.4. The flow is restricted to a channel where there is no normal flow at the meridional walls (at y = 0, L) or at the upper and lower flat plates (at z = 0, D). The Eady model has three assumptions: A constant Coriolis parameter ($\beta = 0$), uniform stratification (N = const.) and a mean velocity with constant vertical shear but no lateral shear (U = Λz).

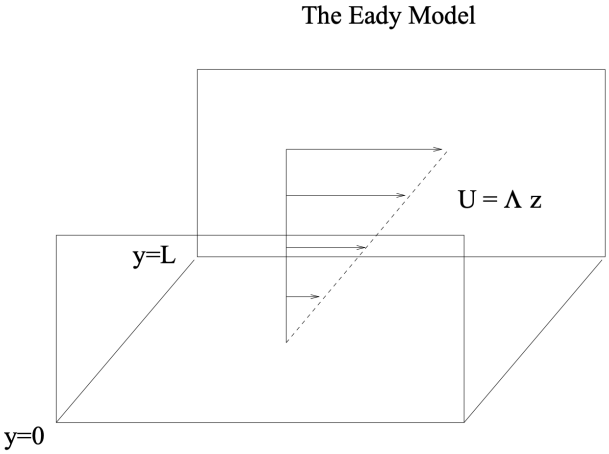

Figure 2.4: Illustation of the Eady model by LaCasce (2020).

The phase speed of a baroclinic wave in the Eady model can be written as:

$$C = \frac{\Lambda D}{2} \pm ic_i, \tag{2.4}$$

where:

$$c_i = \frac{\Lambda}{\alpha}[(\coth[\frac{\alpha D}{2}] - \frac{\alpha D}{2})(\frac{\alpha D}{2} - \tanh[\frac{\alpha D}{2}])]^{1/2}. \tag{2.5}$$

c_i is the imaginary phase speed, Λ is the wind shear and D is the fluid wind shear. The parameter α can be expressed as $\alpha \equiv N\kappa/f_0$, where N is the Brunt-Väisälä frequency, f_0 is the f-plane approximation of Coriolis and κ is the zonal wave number.

In the midpoint of the vertical (the steering level), the waves are propagating at a speed equal to the mean flow speed. At the upper boundary the waves are moving slower than the mean flow, while they are moving faster at the lower. The Eady growth rate of baroclinic waves is expressed as κc_i. As κ increases, the growth rate increases from zero, reaches a maximum value

and then goes to zero again. For κ larger than a critical value, the waves will become stable. The "storm scale" (e.g. the size of a low pressure system) is one half of the wavelength where the growth rate is maximum. A wave of this size is referred to as the most unstable wave. It will grow faster than all the other waves, and will dominate after a period of time.

Even if the Eady model is simplified, it captures many of the essential elements of baroclinic instability. One should still keep in mind that interior PV gradients could affect the stability, and other models such as Charney (1947) and Phillips (1954) take this into consideration (LaCasce, 2020).

Eady parameter

The Eady parameter of maximum growth rate is a commonly used measure of baroclinicity, and descends from linear models like the Eady model. The Eady parameter tells you how fast baroclinic waves amplify, usually given in terms of day^{-1} (Shaw et al., 2016). As mentioned, κc_i is the growth rate of baroclinic waves in the Eady model, so if this parameter is positive the waves will amplify in time. To go from this growth rate to the Eady parameter, we need the growth rate for the most unstable wave to be at its maximum. The baroclinic growth will peak where the baroclinicity of the flow is largest, and the exact mathematical expression from Lindzen and Farrell (1980) is:

$$\Gamma = (\kappa c_i)_{max} = \frac{f}{N}\frac{\partial \overline{u}}{\partial z} \times 0.3125, \tag{2.6}$$

where $\overline{u}$ is the time mean zonal wind, f the Coriolis parameter, N the static stability and the constant 0.3125 comes from $(\alpha c_i)_{max} = 0.3125 \pm 0.0075$. Another form of Equation 2.6 can be found by substituting an approximate form of the thermal wind relation:

$$\frac{\partial \overline{u}}{\partial z} = -\frac{g}{f\overline{T}}\frac{\partial \overline{T}}{\partial y}, \tag{2.7}$$

into Equation 2.6, yielding the following expression:

$$\Gamma = (\kappa c_i)_{max} = -(0.3125 \times \frac{g}{\overline{T}N})\frac{\partial \overline{T}}{\partial y}. \tag{2.8}$$

Equation 2.8 has been used with small modifications by among others Hoskins and Valdes (1990), Chang et al. (2002) and Yin (2005). Even though the expressions vary slightly, the Eady growth rate is in general proportional to the meridional temperature gradient and inversely proportional to the static stability, multiplied by a constant.

Figure 2.5 shows the horizontal distribution of the Eady parameter on the 780 hPa surface, using the expression from Hoskins and Valdes (1990). The storm track entrance regions coincide

with the maxima in the Eady parameter, areas of strong baroclinic growth. These regions are typically found at the core of the tropospheric jets (Chang et al., 2002).

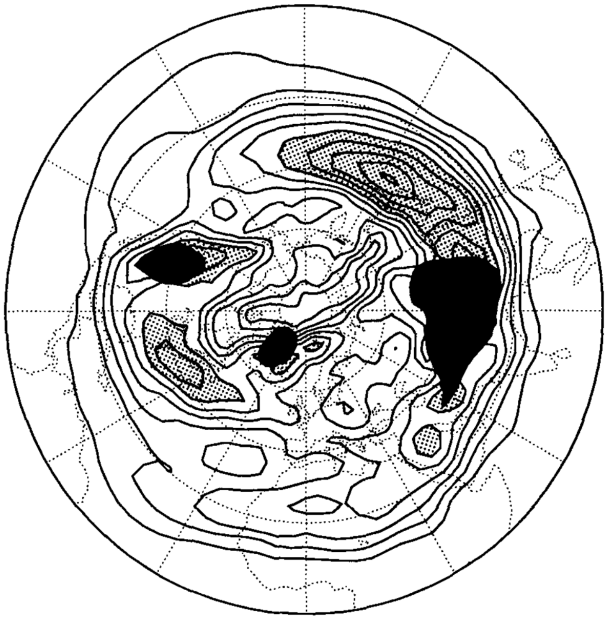

Figure 2.5: Eady parameter ($\Gamma = 0.31 \frac{f}{N} \frac{\partial \overline{v}}{\partial z}$) at 780 mb for the NH winter mean. The contour interval is 0.1 day^{-1} with zero at equator and values below 0.1 day^{-1} at the North Pole. The stippling denotes values in excess of 0.6 day^{-1}. The black areas indicate regions where the 780 mb level is within 1 km of the orography. Figure by Hoskins and Valdes (1990).

2.3 The North Atlantic storm track in previous studies

2.3.1 Previous studies using reanalysis

To know more about long term atmospheric trends, reanalysis products are useful. The IPCC's AR6 points out an overall low confidence for recent changes in global extra-tropical storm tracks due to strong interannual-decadal variability, a range of tracking methods and sensitivity to resolution. Low confidence is also found for the recent changes in cyclone numbers in both hemispheres, while the confidence level for a poleward shift is medium. There is high agreement among reanalyses that the number of intense cyclones (P<970 hPa) has declined during NH winter from 1979 to 2010 (Gulev et al.). AR6 cites a number of studies that look at changes in storm tracks in reanalysis data (e.g. Tilinina et al. (2013) and Chang and Yau (2016)).

Tilinina et al. (2013) compare the characteristics of NH cyclone activity in five different reanalyses for the period 1979–2010 using a single numerical cyclone tracking algorithm. The spatial resolution of the reanalysis is found to strongly affect the total cyclone number. Enhanced cyclone numbers are found for the NA storm track during winter. However, the number of intense cyclones (<960 hPa) increased in NA until 1990, and later declined. A poleward deflection of NH storm tracks in boreal winter is identified during 1979-2010 (Tilinina et al., 2013).

Chang and Yau (2016) study the NH winter storm tracks trends from 1959 to 2010 in six reanalysis datasets and rawinsonde observations. The cyclones are tracked using the objective tracking algorithm of Hodges (1994) on the sea-level pressure (SLP). Similar to Tilinina et al. (2013) they find that the NA storm track has likely increased, here by <10 % from 1959 to 2010.

2.3.2 Climate scenario studies

Climate scenario studies help to understand how storm characteristics will change in future scenarios, e.g. with a quadrupling of CO_2. Similar to AR5, AR6 finds low confidence in regional storm track changes. The number of cyclones is projected to decline in future projections, but only by a few percent. The NA storm track is unlikely to have a simple poleward shift and there is high confidence that average and maximum cyclone precipitation rates will increase with warming. AR6 cites a number of climate scenario studies (e.g. Chang (2018), Yettella and Kay (2017) and Yin (2005)).

Chang (2018) uses 19 models from CMIP5 to study how cyclones producing extreme near-surface winds are projected to change during winter. The models project a decrease in the number of such intense cyclones under the Representative Concentration Pathway 8.5 (RCP8.5) scenario. The RCP refers to the scenarios developed by the IPCC which describe time series of emissions and concentrations of greenhouse gases, aerosols and chemically active gases, plus land use/land cover. The RCP8.5 refers specifically to the high pathway that leads to a radiative

forcing of >8.5 W m^{-2} in 2100 (Moss et al., 2010). In this study, the model mean decrease is found to be of about 21 % for the NA region by the end of the twenty-first century. A similar result is also supported by Seiler and Zwiers (2016) which attribute the decrease to a reduced low-level baroclinicity from SSTs and sea ice changes.

Yettella and Kay (2017) use 30 simulations from the Community Earth System Model Large Ensemble (CESM-LE) to study the precipitation response to global warming. A historical run from 1920 to 2005 is used in addition to the RCP8.5 forcing from 2006 to 2100. The cyclone centers are identified as minima in the daily averaged SLP, following the methods in Serreze (1995). They find increased evidence that precipitation associated with individual cyclones are projected to increase. The increase is mostly attributed to the increase in the atmospheric water vapor. They also find that changes in the wind speeds around cyclone centres are negligible. Even though the projections in intensity from wind speed are projected to be small, a change in the location of the storm track could still lead to changes in local extreme wind speeds. The influence of changes in cyclone numbers on cyclone-associated precipitation is also studied. Similarly to Zappa et al. (2013b) the track density is found to have a tripolar response in NA winter. The pattern is characterized by a decrease in the Norwegian and Mediterranean Seas, while an increase is found for the British Isles. The density response is found to be a result of a reduction in the tilt and an eastward extension of the NA storm track.

Using an ensemble of 15 general circulation models (GCMs), Yin (2005) studies the storm tracks response to an increased greenhouse gas concentration. Figure 2.6 (top figures) illustrates a poleward and upward shift in the Eady parameter in both hemispheres and seasons. However, the shift is partially offset in NH during winter due to a reduced high-latitude surface baroclinicity. The effect of the meridional temperature gradient (middle figures) on the baroclinicity is clearly larger than the effect from the static stability (bottom figures). The shift is found to be strongly linked to the enhanced warming in the tropical upper troposphere and increased tropopause height. The poleward shift is also supported by Tamarin-Brodsky and Kaspi (2017). By applying a storm-tracking algorithm to an ensemble of CMIP5 models based on a Lagrangian view, they bring a new perspective on the shift. They show that in addition to a poleward shift in the genesis latitude of the storms, associated with the shift in baroclinicity, the latitudinal displacement of cyclonic storms increases under global warming. The increased poleward propagation in a warmer climate is shown to be a result of the strengthening of the upper tropospheric jet and increased cyclone-associated precipitation.

Graff and LaCasce (2014) investigate changes in cyclone characteristics as a results of changes in SSTs. The cyclones are identified using 850-hPa relative vorticity from an atmospheric GCM by applying an objective Lagrangian tracking algorithm. The statistics are found by using 20-yr simulations, where the SSTs are warmed or cooled by 2 K in latitudinal bands. Four sensitivity

runs are used; the 2K run, the 2K-lowlat run and the ± 2K-highlat runs. In the 2K run the SSTs were increased uniformly over the oceans, while in the three other runs the SSTs were increased/decreased poleward or equatorward of 45 °. Consistent with Yin (2005) the 2K-lowlat, 2K, and -2K-highlat runs made the mean cyclone positions shift poleward. Similar to Tamarin-Brodsky and Kaspi (2017) the poleward propagation is also expected to increase. The 2K-highlat run, on the other hand, produces a relatively weak response. This is seen in Figure 2.7 from Graff and LaCasce (2012), a study similar to Graff and LaCasce (2014) but here they use BP-filtered geopotential height.

The storm track response to a reduction in sea-ice cover is not straightforward. Various projections are found for the position of the NA storm track. Magnusdottir et al. (2004) use a National Center for Atmospheric Research (NCAR) atmospheric GCM to study the NA region. Two types of forcings are applied; SST anomalies and sea ice anomalies. The decreasing trend in the Labrador and Greenland sea ice produces a weaker storm track that shifts equatorward, which is consistent with a negative NAO response and similar to the 2K-highlat response in Graff and LaCasce (2012). On the contrary, Kvamstø et al. (2004) find that the reduction in the Labrador sea ice tends to shift the storms polewards. It is worth to mention that this is an active science field. Several studies look at how changes in SSTs and sea-ice affect the atmospheric circulation by using experiments under the Polar Amplification Model Intercomparison Project (PAMIP) (Smith et al., 2019). PAMIP can hopefully reduce the uncertainties in future projections by improving our understanding of the physical processes that drive polar amplification.

In summary, AR6 finds low confidence in regional storm track changes. However, some results for the NA region have higher confidence levels. This includes high confidence that more cyclones will be associated with extreme precipitation in the future. Medium confidence is found for a reduction in frequency of the strongest storms. In addition, it is medium confidence that the changes in intensity will be small. When it comes to the density, the total number of cyclones is expected to decease by a few percent. However, where we have the density decrease or increase varies, and there is still a low agreement among CMIP6 models. When studying the position, a simple poleward shift is unlikely for the NA storm track, in contrast to what is found for the NP and Southern hemisphere (SH) storm tracks. Even with small intensity changes, a shift in the storm track position could bring large changes in local extreme winds. Further studies are of interest to understand how the characteristics of the NA storm track will change.

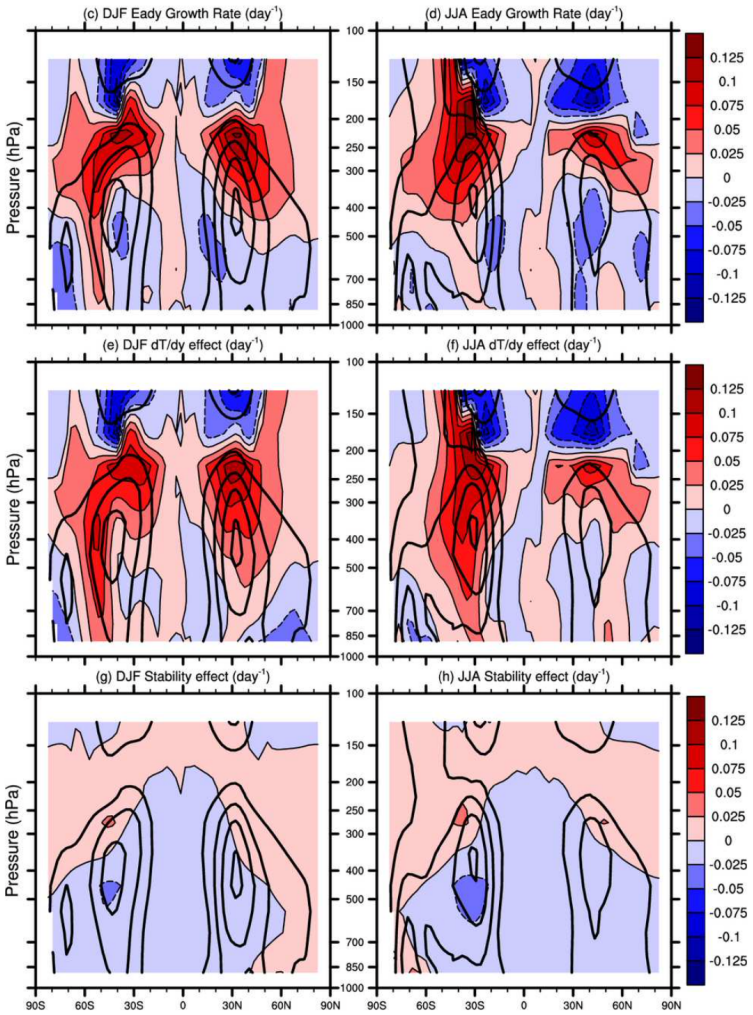

Figure 2.6: Filled color contours represent the zonal mean difference between the scenario runs (with greenhouse gases in accordance with the IPCC climate scenario A1B) and the control runs of (c, d) maximum Eady growth rate ; (e, f) difference in maximum Eady growth rate due to changes in meridional temperature gradient; and (g, h) difference in maximum Eady growth rate due to changes in static stability. The contour interval is given by the color bar in terms of day^{-1}. The left column shows DJF and the right shows June, July and August (JJA). Black contours represent the Eady parameter from the control run, with a contour interval of 0.2/day. Figure is from Yin (2005).

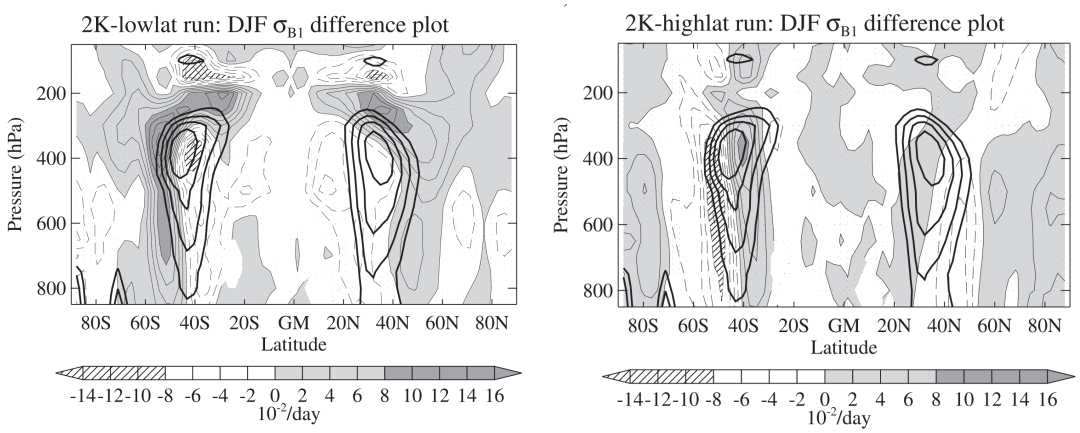

Figure 2.7: Filled color contours represent the zonal mean difference in the maximum Eady growth rate between the control runs and the scenarios for (left) 2K-lowlat run and (right) 2K-highlat run. The contour interval is given by the color bar in terms of day^{-1}. The thick solid (stippled) contours are positive (negative) control run contours (CRCs) for reference, and are 5, 6, 7, and 8 day^{-1}. Figure is from Graff and LaCasce (2012)

3 | Data

This chapter provides information about the model- and reanalysis data, and the related variables used for conducting the analysis in this thesis.

3.1 The NorESM2 model

In this study, the outputs from the Norwegian Earth System Model version 2 (NorESM2), participating in the sixth phase of the CMIP are used (Eyring et al., 2016). This is the second version of the fully coupled Earth system model (ESM), developed by the Norwegian Climate Center (NCC). NorESM2 is based on the second version of the Community Earth System Model (CESM2.1), but has several modifications. It exists in three versions, and the version called NorESM2-MM will be used in this study. The "MM" refers to the medium horizontal resolution ($\sim 1°$) of both the atmosphere–land and the ocean–sea ice components. The land-ice component is inactive, which excludes the melting of land-ice (Seland et al., 2020). An overview of the different components in NorESM2 can be seen in Figure 3.1.

The atmosphere component, Community Atmosphere Model 6 (CAM6) Nor, is built on the CAM6 version. It uses a hydrostatic finite-volume dynamical core on a grid spacing of 1.25° $\times$ 0.9375°. It has 32 hybrid-pressure layers and a "rigid" lid at 3.6 hPa (40 km). A 30 min physics time step is used, with 8-fold dynamics substepping. The ocean model component, the Bergen Layered Ocean Model (BLOM), is based on the Miami Isopycnic Coordinate Ocean Model (MICOM). Its 53 model layers are used with an isopycnic vertical coordinate system, which means a constant potential density except for the two upper layers. These two layers are non-isopycnic and represent the surface mixed layer (Seland et al., 2020). More information about the different model components are given by Seland et al. (2020).

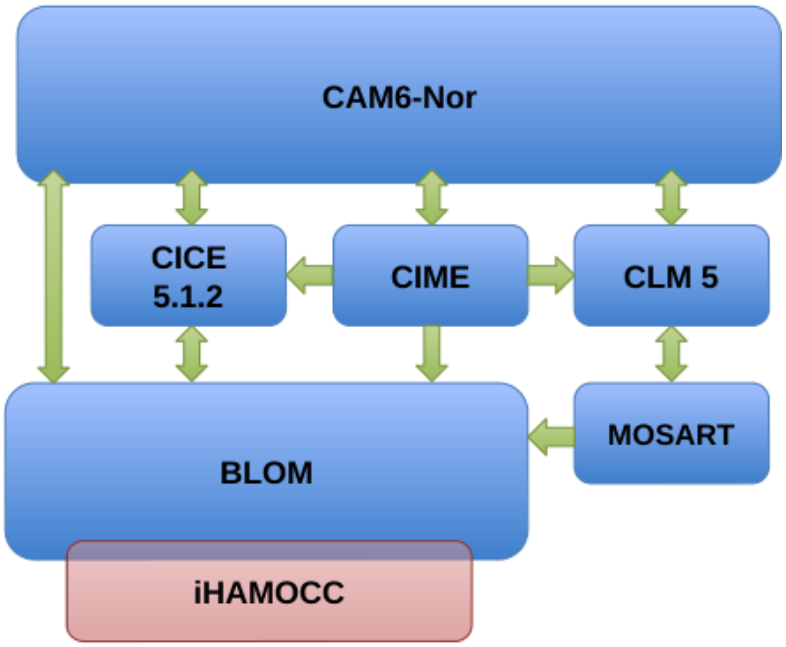

Figure 3.1: Overview of the model components in NorESM2 and how they interact (CIME: configuration handler; CAM6-Nor: atmosphere and aerosol; CICE5.1.2: sea ice; CLM5: land and vegetation, MOSART: river transport; BLOM: ocean; iHAMOCC: ocean carbon cycle). Figure from Seland et al. (2020).

3.1.1 The experiments

The climate models in the CMIP6 framework run a set of different experiments. In this study, four experiments will be explored; the pre-industrial control run (also called piControl), the abrupt-4xCO2 simulation, a historical run (see Eyring et al. (2016)) and a shared socioeconomic pathway (SSP), particularly the SSP5-8.5 (see O'Neill et al. (2016)).

piControl

The piControl run has 1850 as the reference year, making it representative for the period prior to the large industrialization. The concentrations of atmospheric constituents are fixed, meaning that the forcings are held constant. Since there are no occurring changes in either natural- or human-induced forcings, the piControl can be used to study the unforced internal variability of the climate system. In addition, the simulation is used to assess whether the model climate is stable or if it has a residual climate drift (Seland et al., 2020). The simulation starts after the initial spin-up, where the climate comes into balance with the forcing. In NorESM2-MM, the first year is labelled as year 1200. In this study the years 1320 to 1349 are used.

Abrupt-4xCO2

The abrupt-4xCO2 simulation immediately starts by quadrupling the global mean atmospheric CO_2 concentration and then holds the concentration fixed at the quadrupled value. The original CO_2 concentration is taken from the piControl run at year 1200. The only forcing that differs between the piControl run and the abrupt-4xCO2 simulation is the change in CO_2 concentration. Since the increased CO_2 concentration happens all at once, this simulation is convenient when studying how the climate response develops. In addition, the simulation could be used to estimate the equilibrium climate sensitivity (ECS), which is defined as the steady state change in the surface temperature due to a doubling of the atmospheric CO_2 concentration from pre-industrial conditions (IPCC, b). In this study the years 121 to 150 are used.

Historical

The historical simulation is forced by data sets largely based on observations and covers the period 1850-2014. The historical simulation branches from the piControl run, initialized in 1200. The simulation includes both naturally forcings and changes caused by human activities. The historical simulation can be used to assess model ability to simulate climate and to determine if it is consistent with the observations (Eyring et al., 2016). In this study, we use the first ensemble member, with variant label "r1i1p1f1". The data is selected for the years 1980 to 2014.

SSP5-8.5

The model response to future scenarios can be defined by the SSPs. SSPs are a part of the Scenario Model Intercomparison Project (ScenarioMIP), defined under CMIP6. ScenarioMIP gives climate projections that depend on different scenarios which are important to societal concerns. These concerns regard both climate change mitigation and adaptation. O'Neill et al. (2016) give the following definition of SSPs; "SSPs describe alternative evolutions of future society in the absence of climate change or climate policy". SSP5-8.5 assumes an economy based on fossil-fuel and being energy demanding (O'Neill et al., 2016). Under scenario SSP5-8.5, the warming in the period 2090–2099 compared to 1850–1879 reaches 3.9 K in NorESM2-MM (Seland et al., 2020). In this study the years 2071 to 2100 are used.

3.2 ERA-Interim reanalysis

To give an assessment of how accurate NorESM2-MM is, it is compared with a reanalysis (see Knudsen and Walsh (2016) and Booth et al. (2017) for similar comparisons). A reanalysis provides data about the earlier states of the atmosphere. It uses a fixed forecast model where the first guess of the state is found by using the analysis produced in the previous cycle and then

corrects it by assimilating available observations. Combined, it produces a spatially complete and consistent record (Dee et al., 2011).

In this study, the outputs from a reanalysis called ERA-Interim will be used. ERA-Interim is a global atmospheric reanalysis produced by ECMWF. It was initiated in 2006 and provides data from 1. January 1979 to 31. August 2019. The data assimilation (DA) system used is based on a 2006 release of the integrated forecast system (Cy31r2). The system consists of a 4-dimensional variational analysis (4D-Var) and a 12-hour analysis window. The spatial resolution of the data set is roughly 80 km (T255 spectral), and it has 60 levels in the vertical with the top level at 0.1 hPa (Berrisford et al., 2011). In this study the years 1979 to 2016 are used.

3.3 Data variables

A set of variables from the CMIP6 framework are used (see Table B.1 in Appendix B). In addition, the reanalysis variable used was the 6-hourly SLP.

4 | Methods

The methods used to analyse the model and reanalysis output are presented in this chapter. A review of the specific method applied in this study; feature point tracking using the University of Melbourne Cyclone Detection and Tracking Algorithm is given, followed by a short description of the data analysis.

4.1 Cyclone detection and tracking algorithm

To identify and detect cyclones, the 6-hourly SLP outputs from NorESM2-MM and ERA-Interim are put into the Melbourne University Detection and Tracking Algorithm. The algorithm is built on the concepts of feature point tracking (see Section 2.1) and was developed by Murray and Simmonds in 1991 (Murray and Simmonds, 1991a,b). The code-base is actively maintained at the University of Melbourne, and has been updated in 2020. The algorithm is made to track low-pressure systems mainly in the extra-tropics, but some tropical cyclones can also be detected. The algorithm has two main objectives, namely identifying cyclone locations in the given input data set, and connecting the cyclone locations to full cyclone tracks. Further explanations of the detection and tracking scheme are given below, based on Murray and Simmonds (1991a).

4.1.1 Cyclone detection

The cyclone identification scheme locates maxima in the Laplacian of MSLP. If the winds are geostrophic, the Laplacian of the pressure is equal to the relative vorticity. The algorithm seeks grid-points where the Laplacian of the pressure (Equation 4.1) are larger than any of the twelve (selected value) surrounding grid-points, and greater than a prescribed value of zero $(\text{deg.lat.})^2$ at the starting point.

$$\nabla^2 p(x_i, y_j) = p_{xx} + p_{yy}, \tag{4.1}$$

A local minimum pressure is searched for in all of the points. This is done in a repeating manner by looking at one point and using the first and second space derivatives of the pressure

to define an ellipsoid (Figure 4.1). The centre of the ellipsoid then becomes the next point in the repetitive procedure.

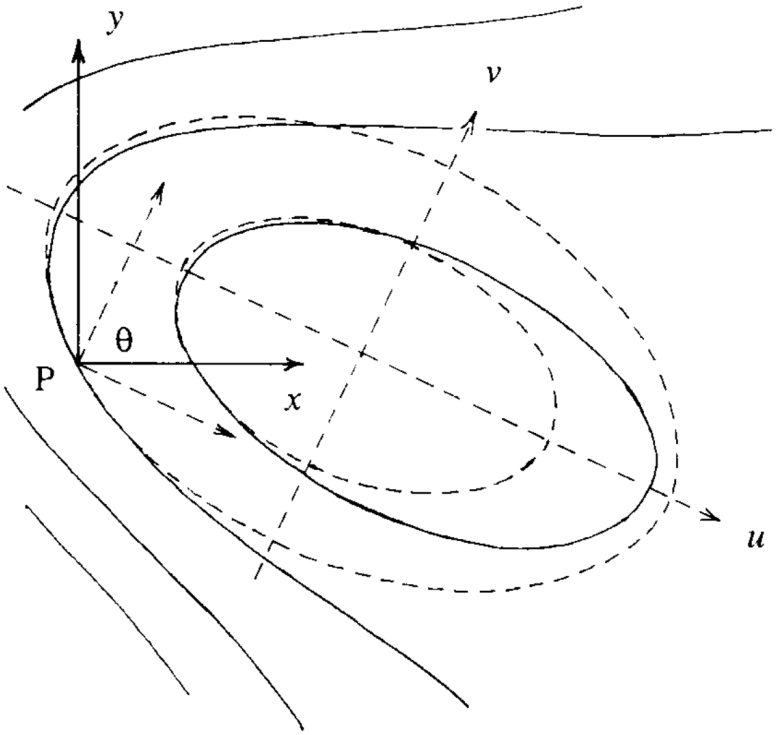

Figure 4.1: Example of a pressure pattern (solid lines) defined by the derivatives at point P. Contours and axes (u and v) of the ellipsoid of best fit (broken lines). Figure from Murray and Simmonds (1991a)

The orientation of the axes , θ, is given by

$$\tan 2\theta = \frac{2p_{xy}}{p_{xx} - p_{yy}}, \tag{4.2}$$

and the second derivatives in the axial directions by

$$p_{uu} = \frac{p_{xx} + p_{yy}}{2} - \sqrt{(\frac{p_{xx} - p_{yy}}{2})^2 + {p_{xy}}^2}, \tag{4.3}$$

$$p_{vv} = \frac{p_{xx} + p_{yy}}{2} + \sqrt{(\frac{p_{xx} - p_{yy}}{2})^2 + {p_{xy}}^2}, \tag{4.4}$$

where u and v are coordinates from the centre of the ellipsoid.

One can refer to low pressure systems as closed or open based on whether they belong to regions of closed isobars or not. If the repetitive procedure described above succeeds to find a minimum, the cyclone is classified as closed, with its core at the point of minimum pressure.

Concerning an open depression, no such point exists, and the point with the minimum pressure gradient (inflexion point) is searched for instead. This particular variable works well since it is normally connected to the concavity in the pressure field. The algorithm searches for an open depression by minimizing the magnitude of the pressure gradient. Finally, the low-pressure system is checked for having the characteristics of a mid-latitude storm. This is done by claiming a minimum value of $\nabla^2 p$ over a specified radius of the cyclone centre (0.4 hPa/(deg.lat.)^2 over a radius of 1.25 deg. lat.) (Murray and Simmonds, 1991a).

The set of cyclone cores resulting from the identification scheme includes many irrelevant systems. Such systems can largely be eliminated by smoothing the pressure field. However, smoothing also eliminates smaller scale cyclones over secondary storm track regions (Pinto et al., 2005). A smoothing radius of 2 degrees has been used in this study.

4.1.2 Cyclone tracking

Based on the results from the identification scheme, a system is tracked from its time of arrival to its dissipation. The most likely position for each cyclone is predicted by using climatological cyclone velocity statistics and the previous movement of the system. The details behind the procedure are explained in Equation 4.5 and illustrated in Figure 4.2.

$$\mathbf{r}_{est}(t+\delta t) = \mathbf{r}(t) + w_M[\mathbf{r}(t) - \mathbf{r}(t-\delta t)] + (1-w_M)\mathbf{v}_{av}(\phi(t))\delta t + \mathbf{r}_K, \tag{4.5}$$

In Equation 4.5 the estimated position ($\mathbf{r}_{est}$) for a time interval (δt) after the current time (t) is obtained. This is done by adding weightings to the current position ($\mathbf{r}$(t)). The second term on the right hand side are weightings of the previous displacements, while the third term are weightings of the displacement based on the assumed climatological average cyclone velocity, for a specific latitude (ϕ). The fourth term $\mathbf{r}_k$ is a small magnitude term which is added to mirror the acceleration implied by the climatological velocities.

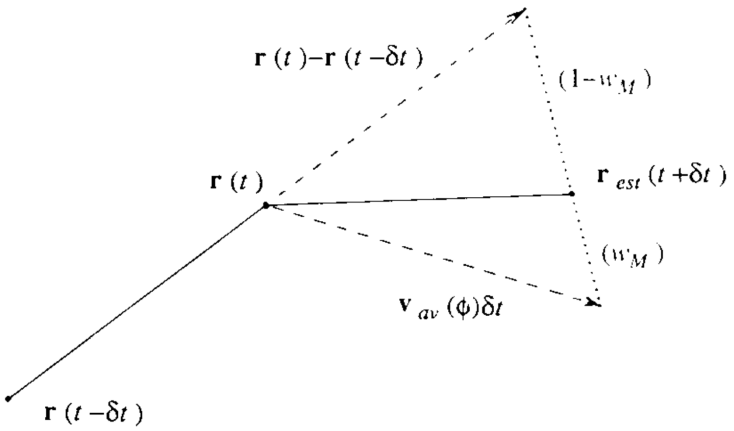

Figure 4.2: Prediction of a new cyclone position ($\mathbf{r}_{est}(t+\delta t)$). Weightings ($w_M$) of the previous displacement ($\mathbf{r}_t - \mathbf{r}(t-\delta t)$) and weightings ($1 - w_M$) of the displacement based on mean cyclone velocities ($\mathbf{v}_{av}(\phi)\delta t$). Figure from Murray and Simmonds (1991a).

The final step of the tracking scheme involves finding probabilities of associations between estimated cyclones and possible candidates as their successors. The probabilities are calculated using a cost function which involves the distance from the estimated position and the difference in core pressures (which could be predicted in the detection scheme) (Pinto et al., 2005). Further details on the final step and the rest of the scheme can be found in Murray and Simmonds (1991a).

4.2 Data analysis

The output from the detection- and tracking algorithm are used to analyse the cyclone characteristics. Storms with lifetime shorter than two days are filtered out, and storms not hitting the defined NA and Scandinavian regions in one or more of its points (Figure 4.3) are excluded. Only storms in the winter months (DJF) are studied.

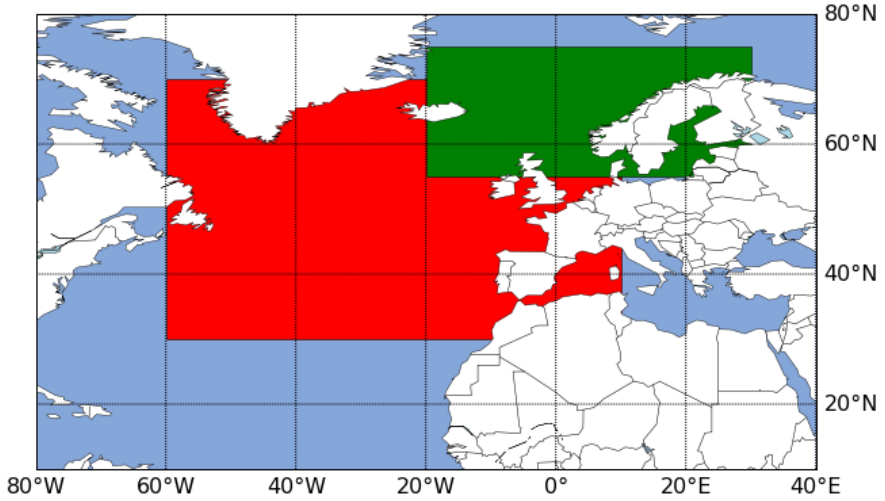

Figure 4.3: Selected regions: NA storms are defined as storms that hit the red box in one or more of its 6-hourly storm centers, while Scandinavian storms have to hit the green box.

4.2.1 Statistics

Once cyclones are identified and tracked, one can calculate statistics, and compare the control runs with different future scenarios. The model statistics are also compared with the ERA-Interim results to see how well the model has performed. Some of the results are presented as histograms and probability density functions, and the statistics for these results are compared with respectively, T-tests and KS-tests (see below).

Probability density function (PDF)

A probability density function describes the probability distribution for a continuous random variable (X). The PDF is non-negative everywhere, and the integral over the total area is equal to 1. The probability for X falling within a particular range a and b can thus be determined by the area under the probability density curve between a and b (Johnson and Bhattacharyya, 2019). In this study we use the function called "gaussian_kde" from the scipy stats module in python (Virtanen et al., 2020). This function uses Gaussian kernels to give a representation of the kernel-density estimate. Out of several possibilities, kernel density estimation is one way to find the PDF. It is found for a random variable in a non-parametic way, and works for both uni-variate and multi-variate data.

T-test

A T-test is used to find the difference between two sample means. If our null hypothesis is that we have equal population means, a p-value smaller than our threshold (here 5 %) will mean that there is a significant difference between the population means. In this study the scipy stats module in python named "ttest_ind" is used, which finds the T-test for two individual sample means (Virtanen et al., 2020). By default, the two-sided test assumes that the samples have identical variances.

KS-test

The KS-test is short for Kolmogorov-Smirnov-test, which is a two-sample test for goodness of fit. The scipy stats module in python named "ks_2samp" is used in this study (Virtanen et al., 2020). The test compares the two samples underlying continuous distributions. The null hypothesis states that the two distributions (PDFs) are identical. A p-value smaller than our threshold (5 %) will mean that there is a significant difference between the distributions, and that they are not identical.

5 | Results

In this chapter, the results from this project are presented. First, the storm characteristics from the NorESM2-MM historical run are compared to the characteristics from ERA-Interim. The second section investigates how the storm track characteristics change by comparing the control runs with the future scenarios; abrupt-4xCO2 and SSP5-8.5. All the following results concentrate on the NH winter season (DJF), thus the winter mean is referred to as the mean.

5.1 Model evaluation

Figure 5.1 shows the mean density of storms in NA in both the model and reanalysis. Overall, the model and reanalysis show similar features. They both observe high cyclone frequencies in the regions where we expect the NA storm track to be located. As mentioned in Section 2.1, storms typically develop in the west and travel east with the jet stream. The southwest-northeast tilt of the NA storm track is visible in this figure for both the model and reanalysis. In NA, a high agreement is found in the cyclone numbers. However, the number of storms is found to be overestimated by around 10 % in Scandinavia. Another feature that stands out is the high density of cyclones west of Iceland, which is visible in both the model and reanalysis. In addition, the model also finds high densities in the Labrador sea. The Mediterranean storm track is also included in the figure, and the model shows a lower density of cyclones than the reanalysis in this region.

Figure 5.2 shows the mean density of storm development in NA, also called the genesis density. Both the model and reanalysis indicate that there are two main areas where the cyclones form; one off the eastern coast of North America, and one near Iceland. The eastern end of the storm track shows low genesis frequencies, as expected, since these regions are often better characterized by cyclone decay. The patterns in the model resembles the ones from the reanalysis. However, the model overestimates the number of storms coming from south of Greenland and underestimates the ones coming from the east coast of North America. The Mediterranean storm track is also evident here as a region of high genesis density.

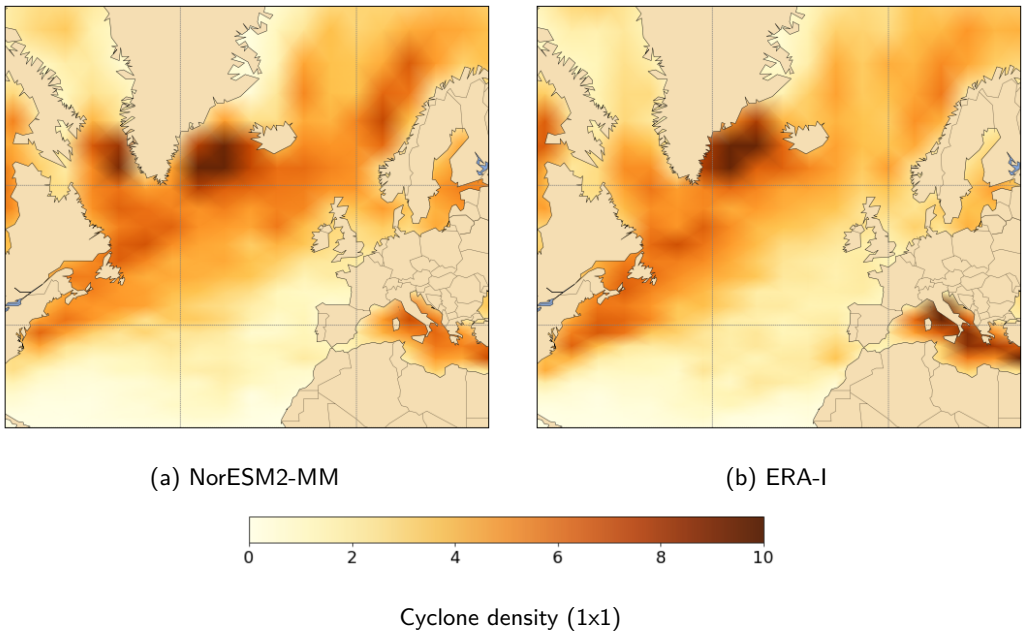

(a) NorESM2-MM (b) ERA-I

Figure 5.1: Mean DJF feature point-density. Calculated by selecting all points in each track, finding the number of DJF storm centers (density) within each 1 x 1 grid cell and dividing by the amount of years. The density is found by using NumPy's 2-D histogram function. Brown areas show where most storms are located for (a) the historical run in NorESM2-MM and (b) ERA-I.

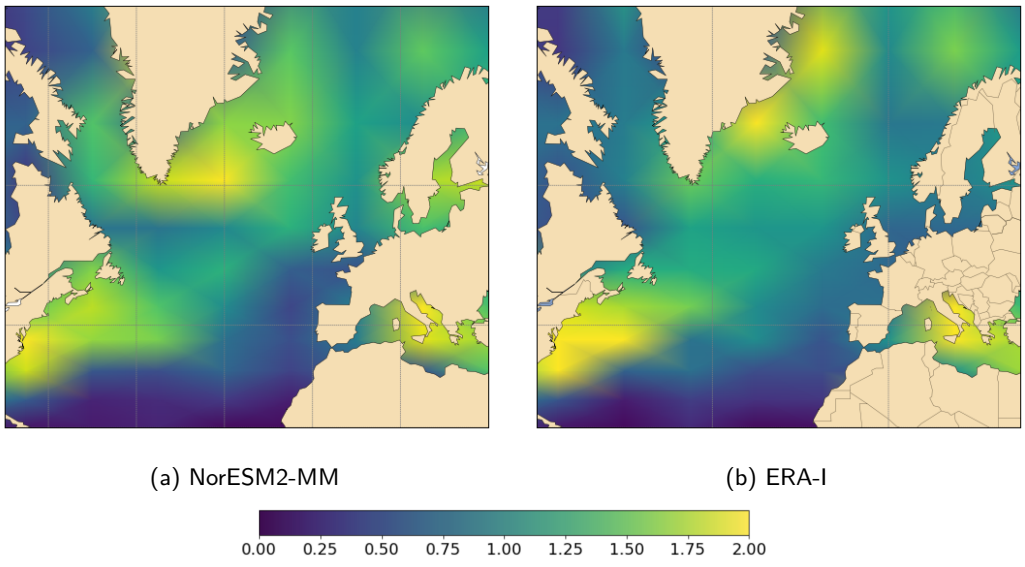

(a) NorESM2-MM (b) ERA-I

Figure 5.2: Mean DJF genesis point-density. Calculated by selecting the first point in each track, finding the DJF density within each 2.5 x 2.5 grid cell and dividing by the amount of years. The density is found by using NumPy's 2-D histogram function. Yellow areas show where most storms are formed for (a) the historical run in NorESM2-MM and (b) ERA-I.

Figure 5.3 shows the mean density of maximum intensity cyclone centers. Both the model and reanalysis exhibit a large number of intense storms in the area from Newfoundland towards Iceland. However, the model underestimates the amount of storms with high intensity, especially in the Mediterranean.

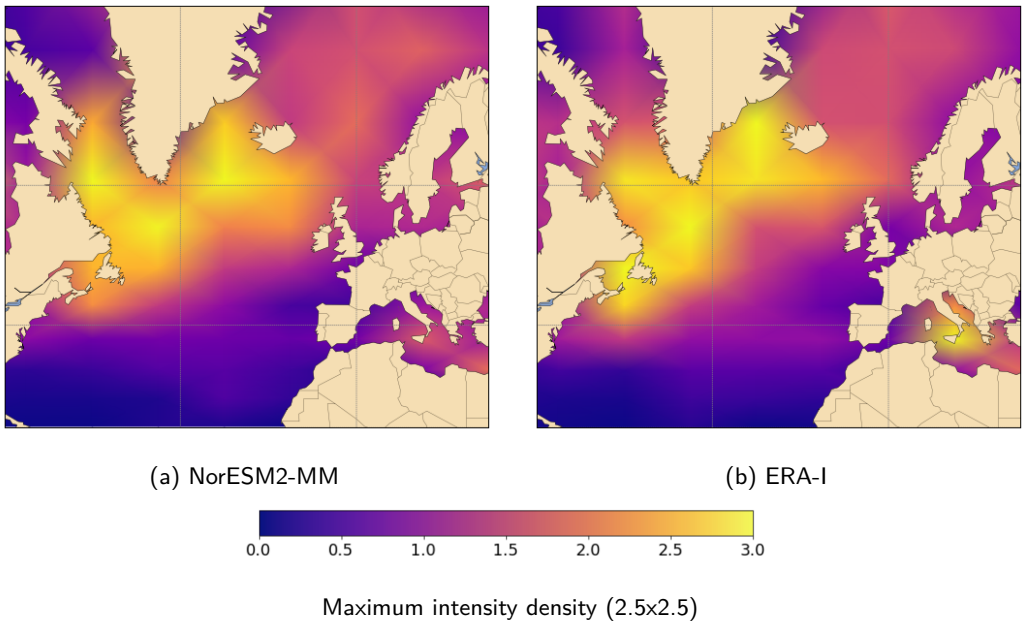

Figure 5.3: Mean DJF intensity (maximum Laplacian) density. Calculated by selecting the point of maximum Laplacian in each track, counting them within each 2.5 x 2.5 grid cell, and dividing by the amount of years. The density is found by using NumPy's 2-D histogram function. Yellow and orange areas show where the highest density of the strongest cyclone centers are found for (a) the historical run in NorESM2-MM and (b) ERA-I during winter.

5.2 Changes in cyclone characteristics

Since the model agrees reasonably well with the reanalysis, we move on to considering how the storm track characteristics change under different scenarios.

5.2.1 The cyclone position

The position of cyclone centers in the NA storm track is found in Figure 5.4. More specifically, it shows the mean point-density for the control runs. It is similar to Figure 5.1, but here we show both of the control runs, so that we get an understanding of the field we compare the scenarios to. The southwest-northeast tilt of the NA storm track is visible, yielding storms from the east coast of North America towards Europe and Scandinavia. The high frequency of cyclones near Greenland is also seen in both of the control runs. The piControl slightly differs from the historical run with less storms west of the United Kingdom.

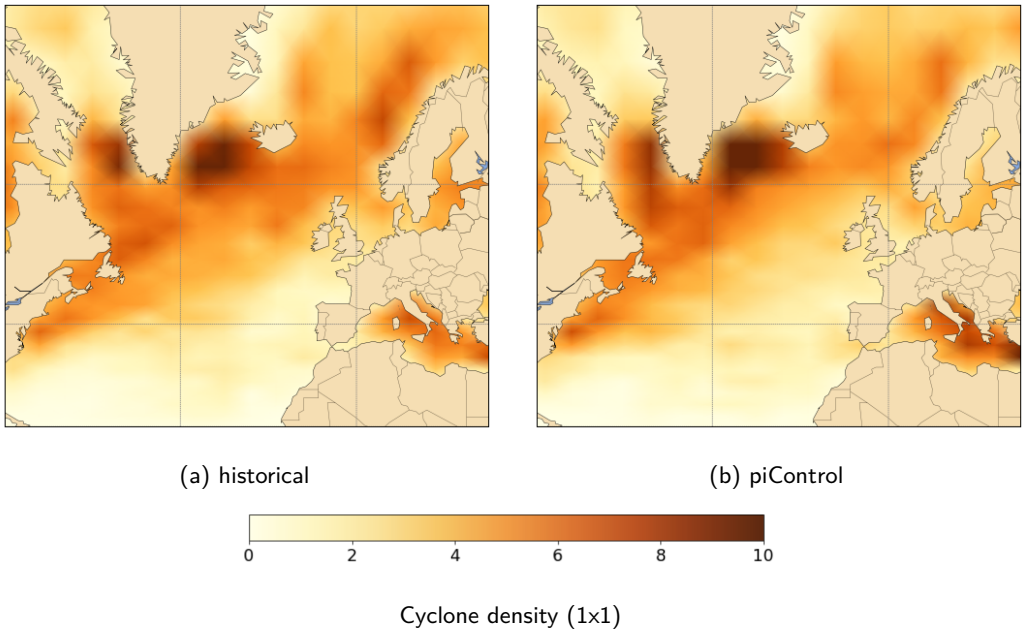

Figure 5.4: Mean DJF feature point-density. Calculated by selecting all points in each track, finding the DJF density within each 1 x 1 grid cell and dividing by the amount of years. The density is found by using NumPy's 2-D histogram function. Stronger colors show where most storm centers are located for (a) the historical run and (b) the piControl run.

Another variable used to study the position of storm tracks is the geopotential height (Blackmon et al., 1977; Yin, 2005; Sampe et al., 2010). As discussed in Section 2.1, areas with large geopotential height variance are associated high cyclone frequencies. The contours in Figure 5.5 represent the 2.5 - 6 days BP-filtered geopotential height variance at 500 hPa. The contours

indicate that we have the highest activity of cyclones near Newfoundland, the area around and towards the northeast. The eastern end of the storm track is associated with a lower variance. The geopotential height variance is a bit different from the point-density as seen in Figure 5.4. Instead of a density maximum over Greenland, the maximum variance is found off Newfoundland.

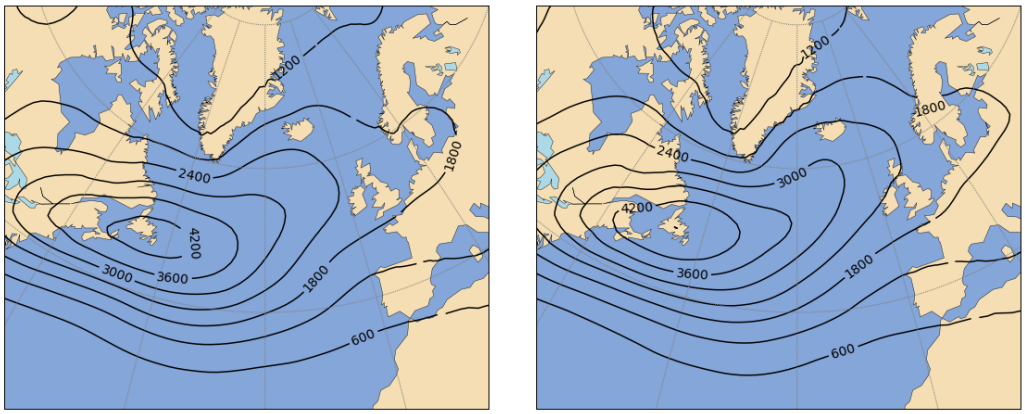

(a) historical (b) piControl

Figure 5.5: The black contours represent the BP-filtered geopotential height variance at 500 hPa [m] for (a) the historical run, and (b) the piControl run. The contours have contour intervals (CIs) of 600 m. The BP-filter (the difference of two lowpass lanczos filters) retain fluctuations between 2.5 and 6 days. A stereographic projection is used (unit: [m]).

Baroclinic growth is dependent on lateral temperature gradients. Hence, it is of interest to study the temperature fields and how they will change. Figure 5.6 shows the zonally averaged mean air temperature anomalies. In both subfigures we see a warm anomaly in the troposphere, and a cold anomaly in the stratosphere. The tropical upper troposphere stands out with its extra warm anomaly. At the surface near the North Pole, we also see positive anomalies, consistent with Arctic amplification. As expected, the abrupt-4xCO2 gives stronger anomalies than the SSP5-8.5.

A commonly used measure for maximum baroclinic growth is the Eady parameter (see Section 2.2.2). A change in the Eady parameter could indicate a change in the rate of storm formation, and in its location. Figure 5.7 shows the zonally averaged mean Eady parameter anomalies. The Eady parameter is calculated using the formula $\sigma_{B1} = 0.31 \times \frac{g}{TN} \times |\frac{\partial T}{\partial y}| \times 0.1$, which is similar to Equation 2.8. Here T is the time- and longitudinal mean of the winter air temperature (ta). The Brunt-Väisälä frequency is calculated as $N^2 = -(g^2 \times p)/(R \times \theta^2) \times (p/p_0)^{(\frac{R}{c_p})} \times \frac{\partial \theta}{\partial p}$, where potential temperature is defined as $\theta = ta \times (p_0/p)^{(\frac{R}{c_p})}$. The constants of R, p_0 and c_p refers to the gas constant for dry air, the surface pressure and the specific heat capacity which are 287 $[\frac{J}{Kg \times K}]$, 1000 [hPa] and 1004 $[\frac{J}{Kg \times K}]$, respectively. A poleward shift could for example be

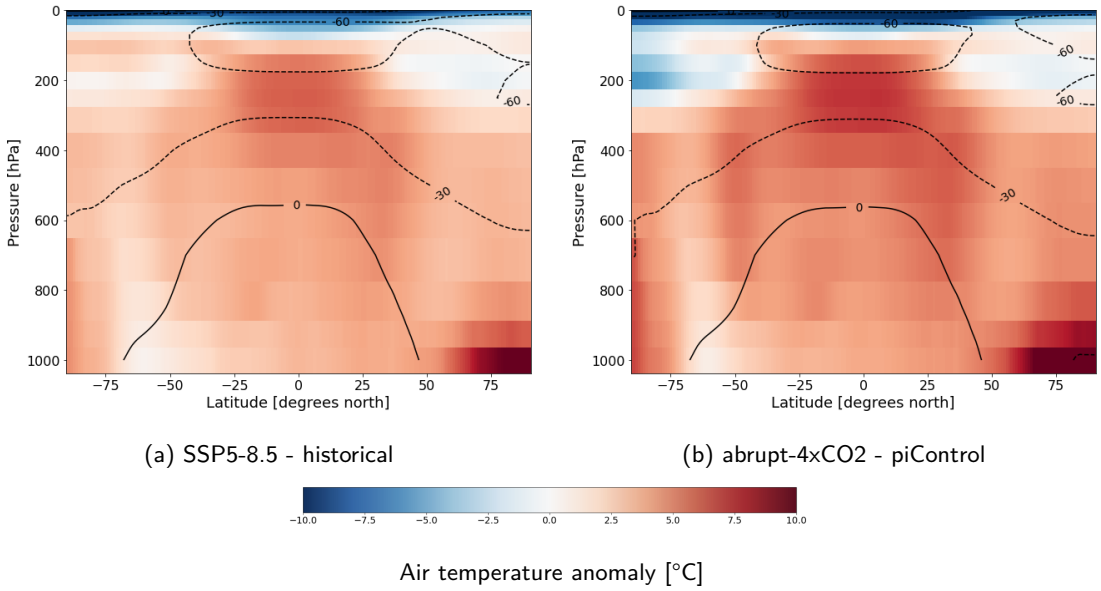

Figure 5.6: Zonally averaged mean DJF air temperature anomalies for (a) SSP5-8.5 - historical and (b) abrupt-4xCO2 - piControl. The black contours represent the climatology of (a) the historical run and (b) the piControl, with CIs of 30 °C. Dashed lines are negative values while solid lines are positive. Red colors represent warmer and blue colder anomalies (unit: °C).

observed by seeing a positive Eady parameter anomaly on the poleward flank of the contours. The only place this is clear is in the SH in the abrupt-4xCO2 anomaly, where a positive anomaly extends downwards into the troposphere. In the NH there is no clear shift for either of the anomalies. The strongest anomalies are found at around 200 hPa, at jet levels. Further down in the troposphere the anomalies are weak.

Averaging with latitude in the Eady parameter could obscure the changes, due to the tilt of the storm track. Thus, we continue to investigate how the position of the storm track will change by studying surface temperatures instead. Figure 5.8 shows the mean surface temperature climatologies and anomalies. As discussed in Section 2.2.1, differential solar heating sets up a meridional temperature gradient which is decreasing from the equator towards the poles. As for the anomalies, we can observe warmer surface temperatures in all regions except the area south of Iceland, for both the SSP5-8.5 and abrupt-4xCO2 scenarios. The Arctic is also found to heat more than the other regions, which is expected due to Arctic amplification. With temperatures anomalies of up to 15-20 degrees, the abrupt-4xCO2 anomaly is stronger than the SSP5-8.5. The strongest anomalies are found over the North American continent, towards Canada and the Labrador Sea. In addition, a strong warm anomaly is found north of Iceland.

Warmer surface temperatures in the Arctic are associated with more sea-ice loss. Figure 5.9 shows the mean anomalies of sea ice concentration. Dark blue areas show where we have the

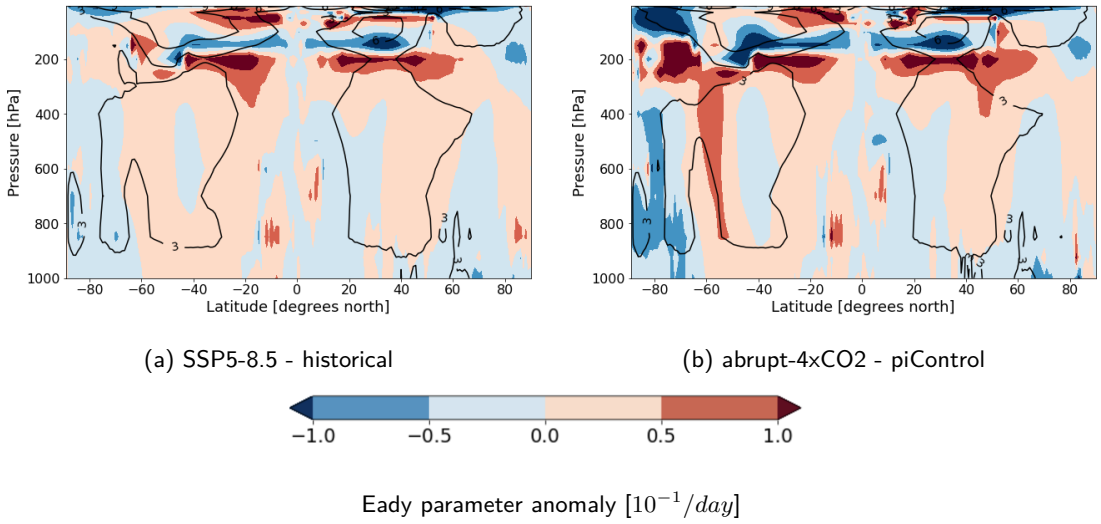

Figure 5.7: Zonally averaged mean DJF eady parameter anomalies for (a) SSP5-8.5 - historical and (b) abrupt-4xCO2 - piControl. The black contours represent the climatology of (a) the historical run and (b) the piControl, with CIs of $10 \times 10^{-1}/day$. Red colors represent an increased Eady parameter, while blue represent a decreased (unit: $10^{-1}/day$).

largest sea ice loss, which coincide well with where we have the strongest surface temperature anomalies. These regions are seen in the Hudson Bay and the area north of Iceland. The loss is larger for the abrupt-4xCO2 anomaly, where the sea ice in some areas disappears completely. The SSP5-8.5 do have some positive sea-ice concentration anomalies around Svalbard and Iceland, consistent with the negative surface temperature anomalies there. However, one should note that these anomalies are weak.

The cold anomaly south of Iceland in Figure 5.8 is referred to as the cold blob. Strong temperature contrasts in the areas of large sea ice loss are evident, e.g. in the Labrador Sea. Here you can see a distinct line between the warm and cold anomalies. The cold blob also extends southward in the Gulf stream area, yielding strong temperature contrasts in areas further south. The blob increases the negative temperature gradient, as opposed to Arctic amplification which weakens it. Thus, we get a more complex situation than explored by e.g. Graff and LaCasce (2014).

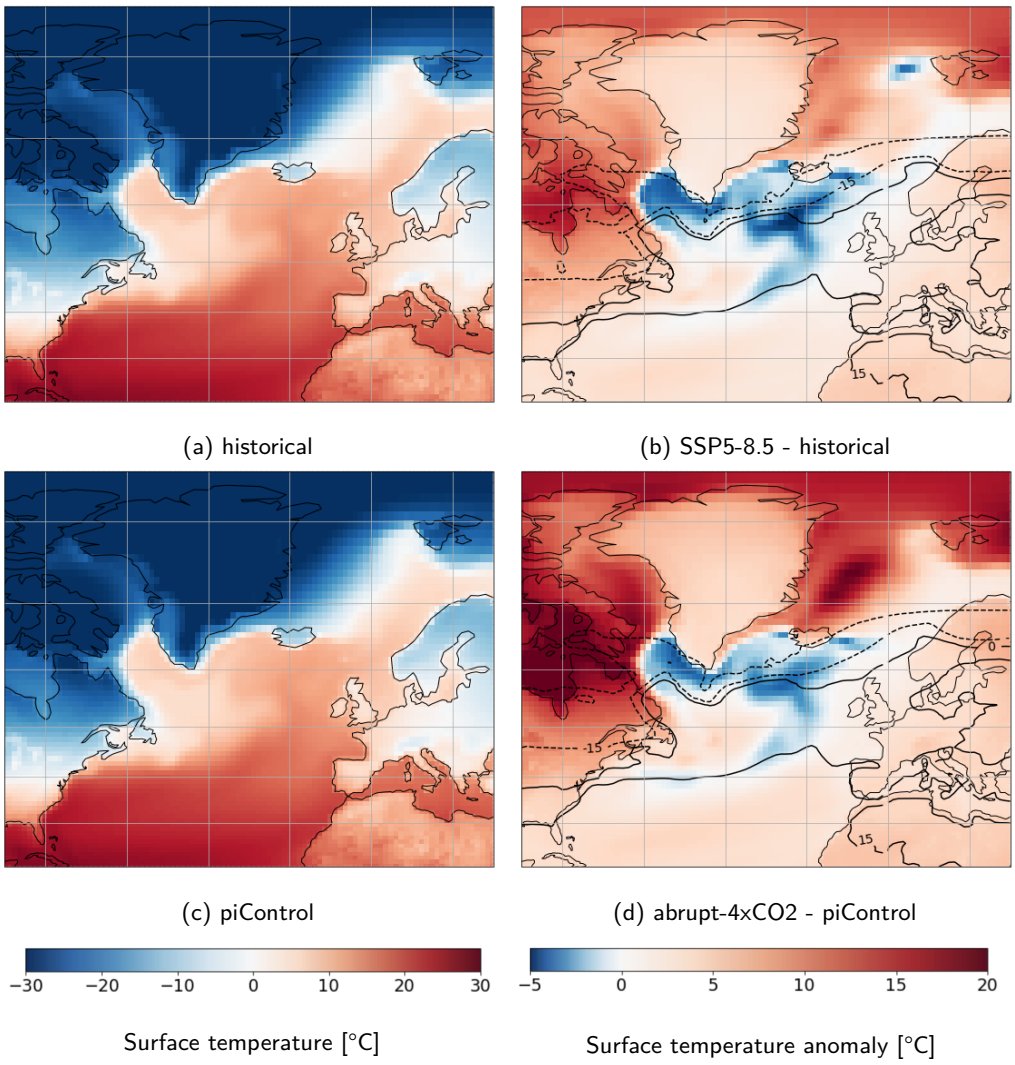

Figure 5.8: Mean DJF surface temperature for (a) historical and (c) piControl and anomalies for (b) SSP5-8.5 - historical and (d) abrupt-4xCO2 - piControl. The black contours represent the climatology of (a) the historical run and (b) the piControl, with CIs of 15 °C. Dashed lines are negative values while solid lines are positive. For the anomalies the red colors represent warmer anomalies and blue colder (unit: °C).

Cyclones typically form in areas with large horizontal temperature gradients. Equation 2.8 reflects how the meridional temperature gradient dT/dy is linked to the genesis. We see that when dT/dy is negative we have a positive Eady parameter, and the baroclinic waves then amplify in time. Figure 5.10 shows where we have the main genesis areas and the associated meridional temperature gradients for the control runs. As in Figure 5.2, we find two main genesis areas, one south of Iceland and one off the east coast of North America. The right column of the figure shows the meridional temperature gradients. Here we find that the two genesis regions

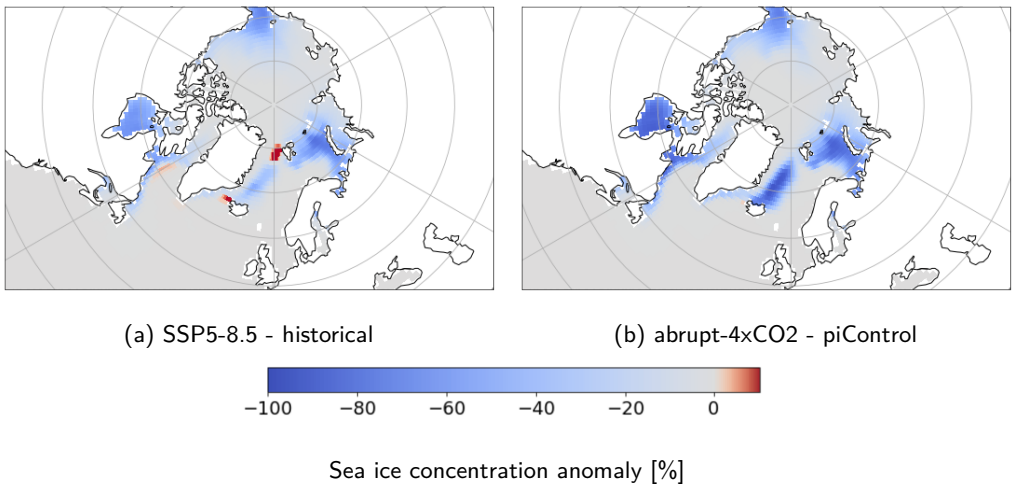

Figure 5.9: Mean DJF sea ice concentration anomalies for (a) SSP5-8.5 - historical and (b) abrupt-4xCO2 - piControl. The North Polar Stereographic projection is used after conservative regridding is done (unit: %).

are characterized by negative local meridional temperature gradients, which is what we expected from Equation 2.8. The area in between the main genesis areas, close to the Newfoundland and Labrador coast, is however characterized by positive meridional temperature gradients and less genesis. To understand how the storm track will change in position we need to know how the starting point of the storm track, the genesis, will change. Where will we have more/less genesis? Will we get a shift? If yes, will the shift be polewards or equatorwards? Understanding how the meridional temperature gradients change could help explain a potential change in position.

To check if we have more or less genesis, the mean genesis point-density anomalies are shown in the left column in Figure 5.11. Here we see that the typical genesis areas near Iceland and the east coast of North America, illustrated in Figure 5.10, have decreased genesis numbers. On the contrary, the area in between the typical genesis regions has increased genesis numbers. In addition, we find more genesis in the Labrador Sea and the Hudson Bay. The right panels in Figure 5.11 show the meridional temperature gradient anomalies. Comparing these panels with the left panels, we see that the areas with increased genesis have negative meridional temperature gradient anomalies. On the other hand, the regions with decreased genesis are associated with positive gradient anomalies. To better understand how the gradient will influence the genesis we compare the right panels in this figure with the right panels in Figure 5.10. Here, we see that where the temperature gradient anomalies are positive, we have negative gradients in the climatologies. This indicate that we get a more positive gradient. From Equation 2.8 we know that a more positive gradient will lead to less genesis in the regions below 40 and above 60 °north due to weaker baroclinicity. The opposite applies for for the region in between, where we have a

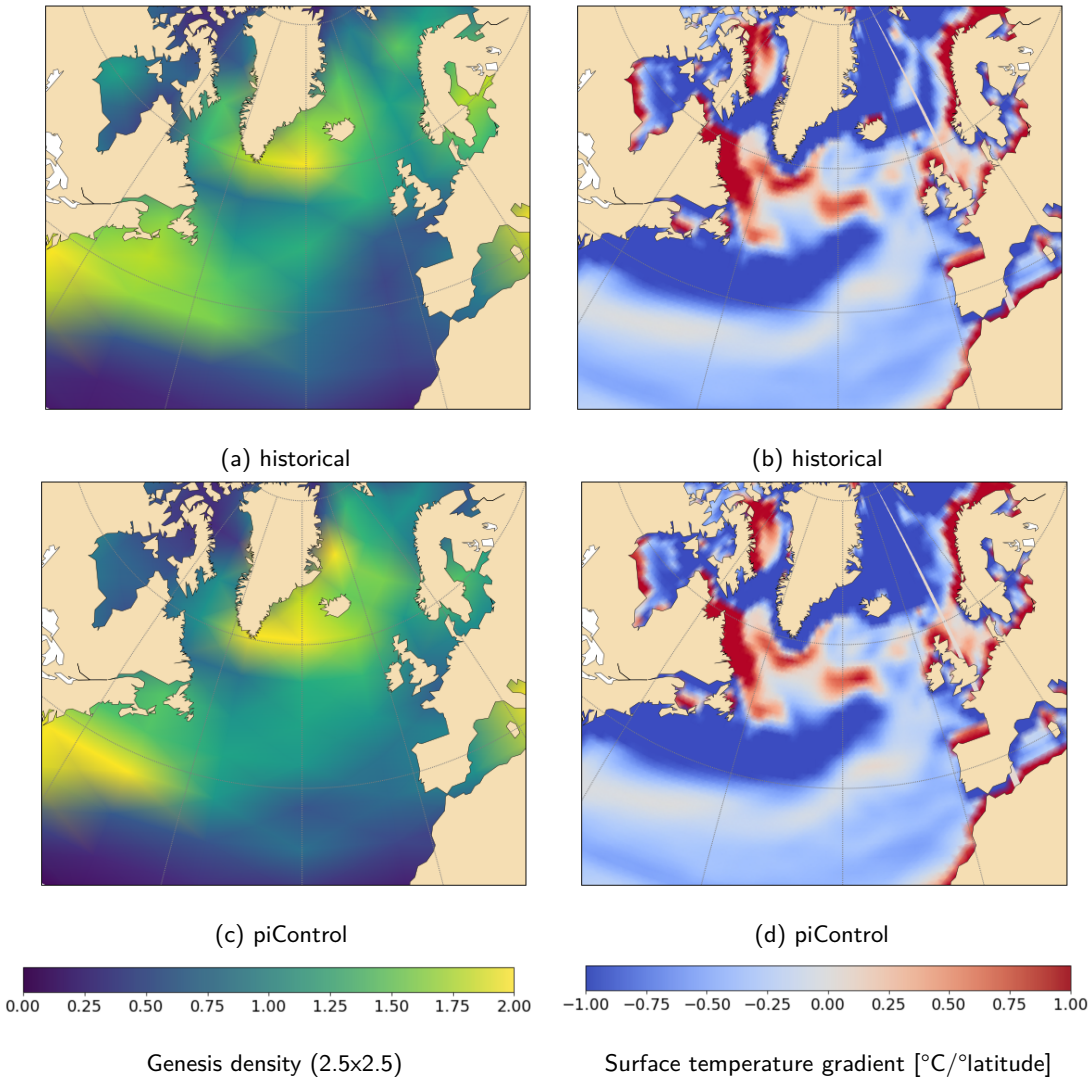

Figure 5.10: The mean DJF genesis point-density climatologies are seen for (a) historical and (c) piControl. Calculated by selecting the first point in each track, finding the DJF density within each 2.5 x 2.5 grid cell and dividing by the amount of years. The density is found by using NumPy's 2-D histogram function. Yellow areas show where most storms are formed. The mean DJF meridional surface temperature gradient climatologies are represented by the filled contours in (b) historical and (d) piControl. The red colors represent a positive meridional gradient, and blue a negative. The Stereographic projection is used.

negative anomaly and positive climatology. The gradient becomes more negative, and thus we get more genesis here.

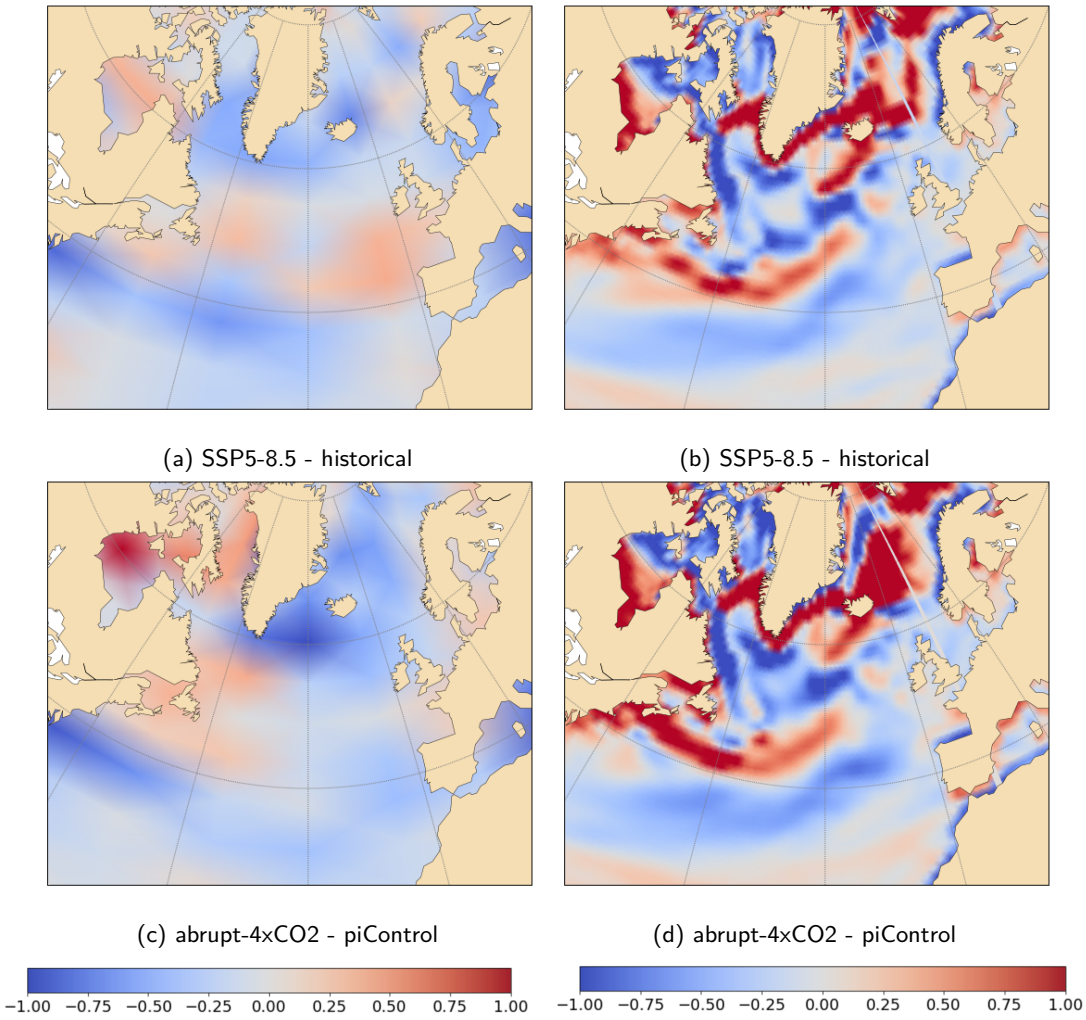

Figure 5.11: The mean DJF genesis point-density anomalies are seen for (a) SSP5-8.5 - historical and (c) abrupt-4xCO2 - piControl. Calculated as in Figure 5.10, but here we find the difference in density of genesis centers per 2.5 x 2.5 grid cell. Red areas show where we have an increase in genesis density, while blue indicate where we have a decrease. The mean DJF meridional surface temperature gradient anomalies are represented by the filled contours in (b) SSP5-8.5 - historical and (d) abrupt-4xCO2 - piControl. The red colors represent an increased gradient, and blue a decreased. The Stereographic projection is used.

To look more into the statistics, we include Figure 5.12 which shows the PDFs for the genesis latitudes. The top figures show the PDFs in NA for the two scenarios. In this region the PDFs are not significantly different, according to the KS-test using a 95 % confidence interval. However, the storms reaching Scandinavia show a significant difference in the genesis latitude between the control runs and the scenarios. Here, the storms in the scenarios are found to be born further south, more specifically, in the region between 35 to 55 degrees north. This corresponds to the tripole structure we found in Figure 5.11, showing fewer storms off the east coast of United States and Greenland, but more off Newfoundland. No significant changes were found in the PDFs for the lysis latitudes (except for SSP5-8.5 in NA which show more lysis in mid- to high latitudes) (see Appendix A).

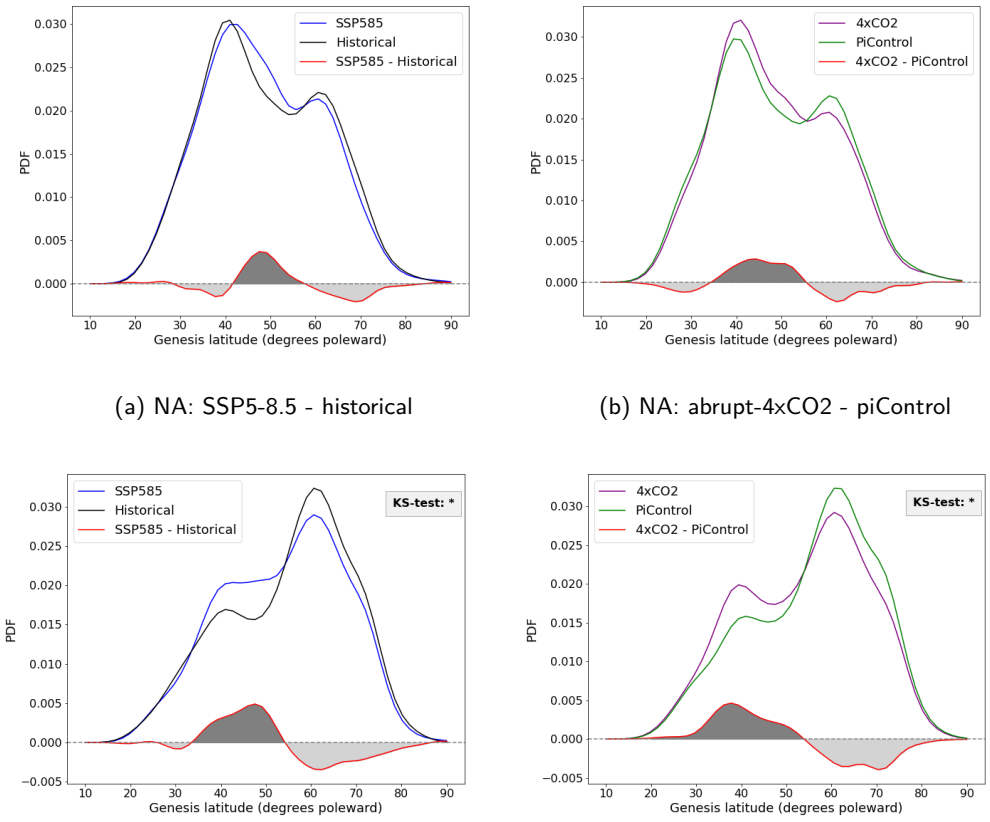

(a) NA: SSP5-8.5 - historical

(b) NA: abrupt-4xCO2 - piControl

(c) Scan.: SSP5-8.5 - historical

(d) Scan.: abrupt-4xCO2 - piControl

Figure 5.12: Probability density functions of genesis latitude. The top row represent NA, and the bottom row Scandinavia. Figure (a) and (c) represent the SSP5-8.5 - historical anomaly while (b) and (d) the represent the abrupt-4xCO2 - piControl. Calculated by choosing the first point in each track during DJF, and selecting the corresponding latitudes. PDFs of the genesis latitudes are then calculated using the "gaussian_kde" module from scipy stats. The KS-test is performed with the "ks_2samp" module.

5.2.2 The cyclone number

An overall reduction in genesis numbers is seen in Figure 5.11. The yearly winter occurrences of storms in the different experiments for the two regions are seen in Figure 5.13. Comparing the winter means of the control runs to the scenarios we see a decrease of roughly 10 % for both scenarios and regions. The specific numbers are found in Table 5.1.

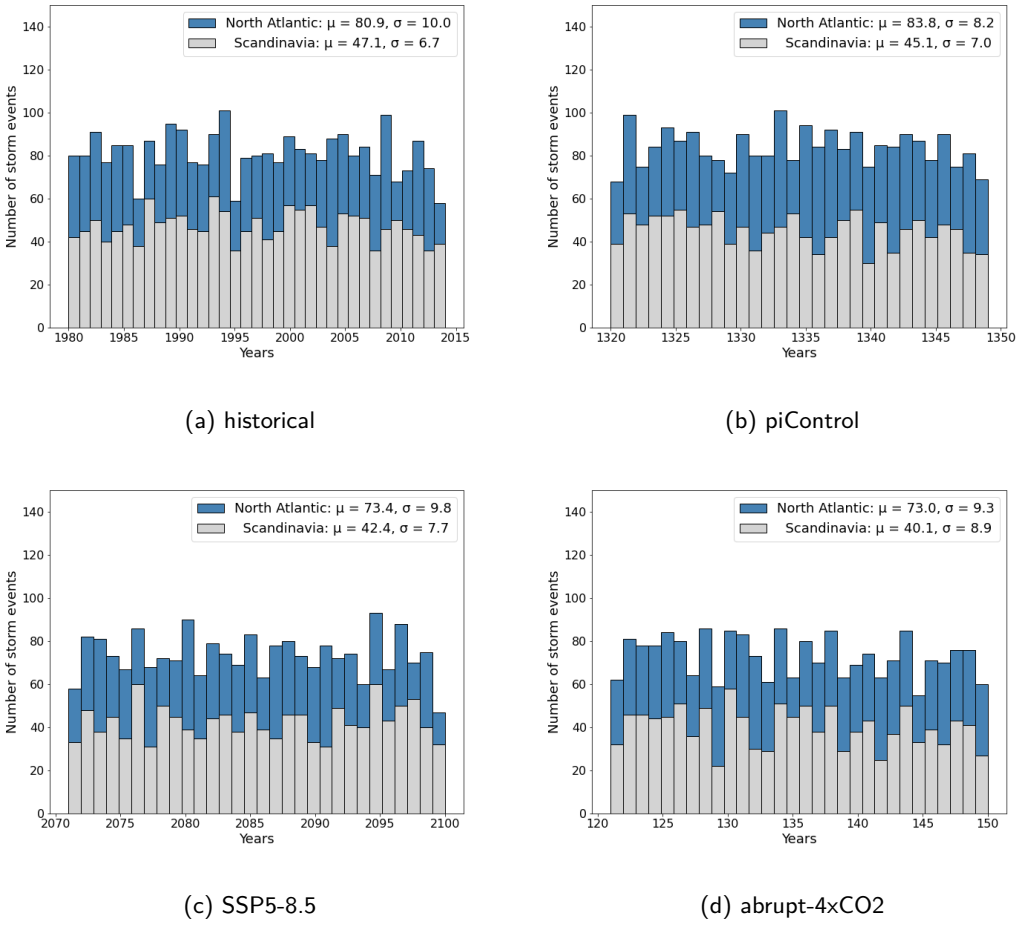

(a) historical

(b) piControl

(c) SSP5-8.5

(d) abrupt-4xCO2

Figure 5.13: Number of storms in NA (blue) and Scandinavia (grey) for (a) the historical run, (b) the piControl run, (c) the SSP5-8.5 scenario and (d) the abrupt-4xCO2 scenario. Calculated by using the genesis numbers and the histogram function in python. The mean and standard deviation are shown in the figure.

Table 5.1: The number of winter storms in NA and Scandinavia.

Mean number of storms DJF	North Atlantic	Scandinavia
historical	80.9	47.1
SSP5-8.5	73.4 (-9 %)*	42.4 (-10 %)*
piControl	83.8	45.1
abrupt-4xCO2	73.0 (-13 %)*	40.1 (-11 %)*

Significant T-test denoted by *

5.2.3 The cyclone displacement

In addition to the temperature gradients, the jet stream also influences where the cyclones travel and their speed (Shaw et al., 2016). Figure 5.14 shows the mean windspeed anomalies at 300 hPa. The contours, which represent the climatologies, show a southwest-northeast directed tilt with a maximum off the east coast of North America. High windspeeds are also found further east towards Europe. The anomalies show increased windspeeds east to northeast of the maximum jet regions, and reductions elsewhere. The abrupt-4xCO2 display a stronger anomaly than SSP5-8.5, and it extends farther over Europe.

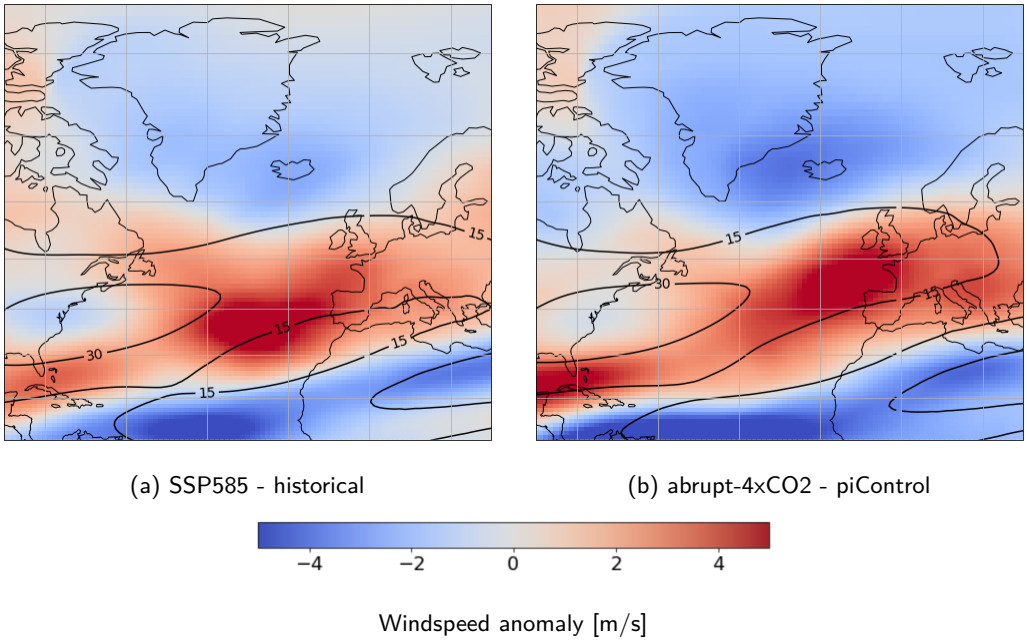

Figure 5.14: Mean DJF windspeed anomalies at 300 hPa for (a) SSP5-8.5 - historical and (b) abrupt-4xCO2 - piControl. The black contours represent the climatology of (a) the historical run and (b) the piControl, with CIs of 15 m/s. Red colors represent stronger wind anomalies and blue weaker (unit: m/s).

Figure 5.15 shows the PDFs for the latitudinal displacement. Both regions and scenarios (except abrupt-4xCO2 in NA) show an increased latitudinal displacement. In other words, the meridional travel distance between genesis and lysis for the cyclones increases in the scenarios. We see the strongest signals for the Scandinavian storms. This agrees well with the previous results, where the Scandinavian storms were found to form further south but not found to change in lysis. This is consistent with a longer latitudinal displacement, and greater advection by the jet. Figure 5.16 shows the PDFs for the longitudinal displacement. Here, only the NA storms show significant changes. For this region an increased longitudinal displacement is found. The lifetime of cyclones was also examined, but showed no significant change in the scenarios (except

SSP5-8.5 in Scandinavia which showed longer lifetimes) (see Appendix A). Since the lifetimes are unchanged and the cyclones travel farther, it it considered that they also travel faster.

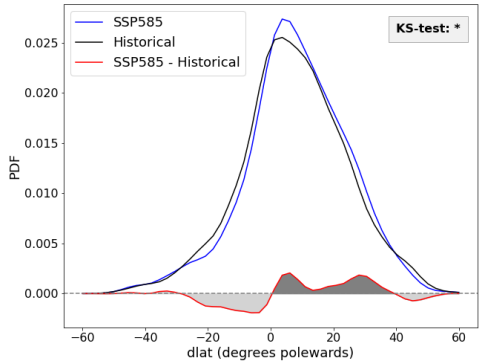

(a) NA: SSP5-8.5 - historical

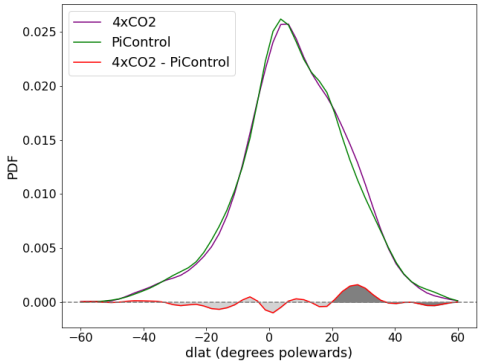

(b) NA: abrupt-4xCO2 - piControl

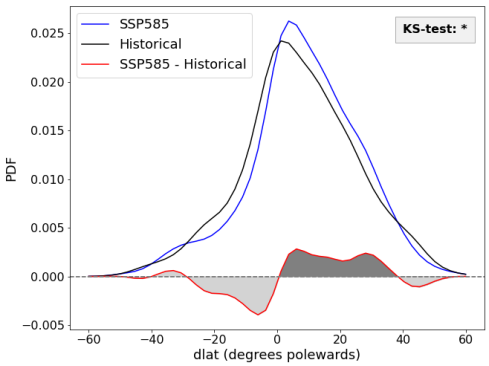

(c) Scan.: SSP5-8.5 - historical

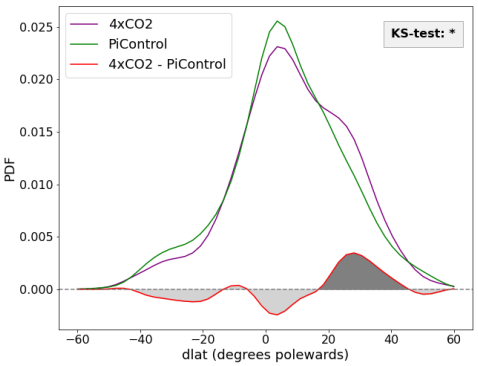

(d) Scan.: abrupt-4xCO2 - piControl

Figure 5.15: Probability density functions of latitudinal displacement. The top row represent NA, and the bottom row Scandinavia. Figure (a) and (c) represent the SSP5-8.5 - historical anomaly while (b) and (d) the represent the abrupt-4xCO2 - piControl. Calculated by selecting the first and last point in each track during DJF, and finding the difference between the corresponding latitudes. PDFs of the latitudinal displacement are then calculated using the "gaussian_kde" module from scipy stats. The KS-test is performed with the "ks_2samp" module.

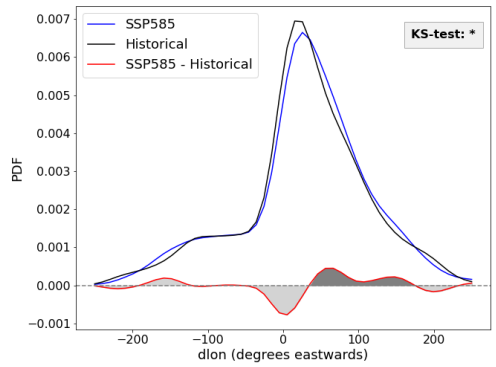

(a) NA: SSP5-8.5 - historical

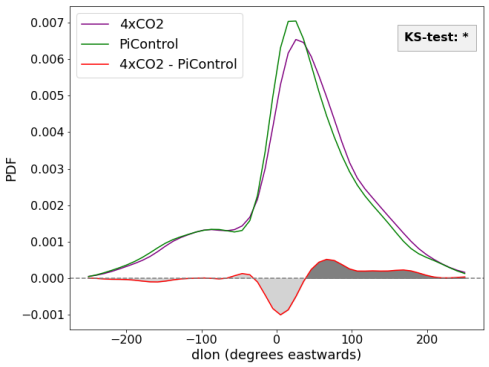

(b) NA: abrupt-4xCO2 - piControl

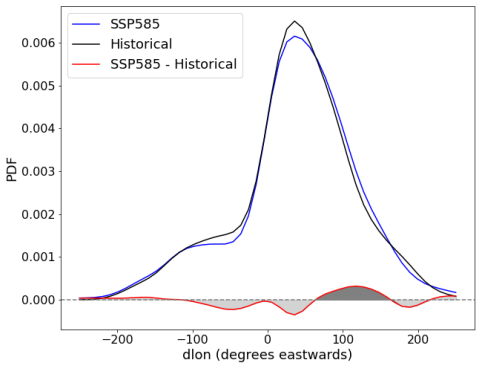

(c) Scan.: SSP5-8.5 - historical

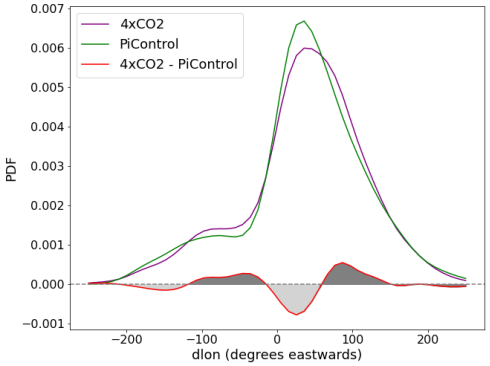

(d) Scan.: abrupt-4xCO2 - piControl

Figure 5.16: Probability density functions of longitudinal displacement. The top row represents NA, and the bottom row Scandinavia. Figure (a) and (c) represent the SSP5-8.5 - historical anomaly while (b) and (d) represent the abrupt-4xCO2 - piControl. Calculated by selecting the first and last point in each track during DJF, and finding the difference between the corresponding longitudes. PDFs of the longitudinal displacement are then calculated using the "gaussian_kde" module from scipy stats. The KS-test is performed with the "ks_2samp" module.

5.2.4 The cyclone intensity

More intense storms in the future could lead to larger socioeconomic impact, thus it is of interest to study whether the intensity of cyclones will increase or decrease. In this study, the intensity is measured in the Laplacian of the pressure due to inconclusive results when using the MSLP. Figure 5.17 shows the geographical distribution of maximum intensity. The distribution is found by identifying the maximum Laplacian for each cyclone and then calculating the mean intensity for each grid cell. The strongest intensities are found in the yellow areas, which is located off the east coast of North America and the area to the northeast. By taking the mean of each grid cell we might exclude the strongest intensities, thus the intensities are quite similar over large areas.

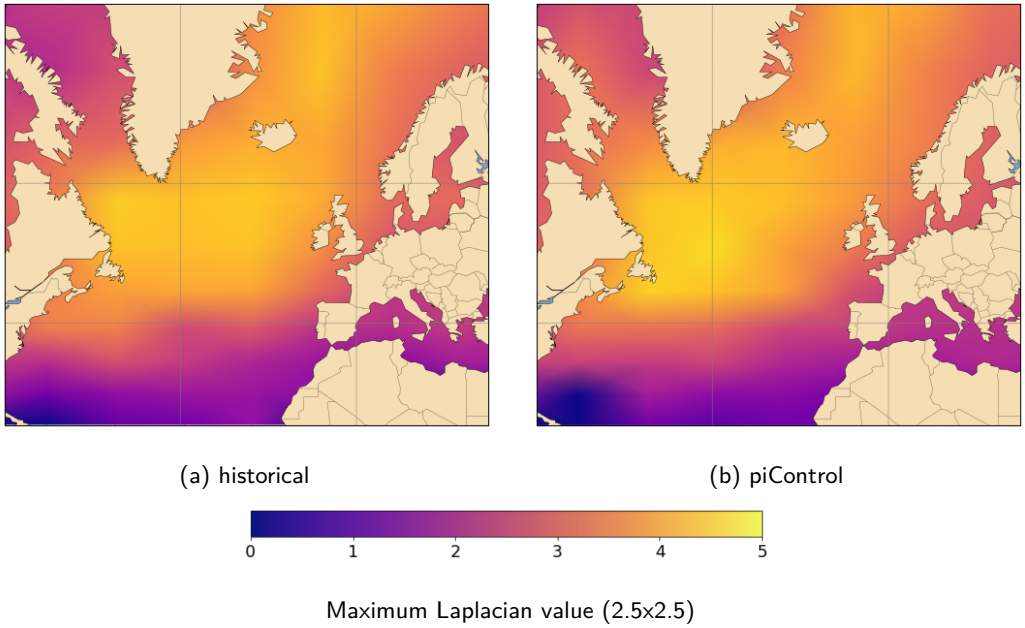

Figure 5.17: Mean DJF intensity (maximum laplacian). Calculated by selecting the point of maximum laplacian in each track, finding the mean intensity within each 2.5 x 2.5 grid cell and thereafter dividing by the amount of years. Yellow and orange areas show where the most intense storms are located for (a) the historical run and (b) the piControl run.

Studying the PDFs of the cyclone intensities can reveal how the intensity will change in future scenarios. Figure 5.18 shows the PDFs of the intensity in maximum Laplacian. Both regions and anomalies (except SSP5-8.5 in NA) show a significant change in the intensity. They all show that we will have more weak storms. In addition, there will be fewer intermediate intensity storms.

Changes in cyclone intensities could affect the precipitation, as weaker storms often are consistent with less precipitation. Figure 5.19 shows the precipitation anomalies during winter. The pattern closely resembles surface temperature. We get less precipitation south of Iceland,

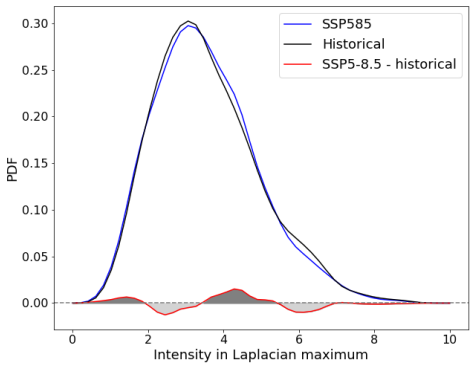

(a) NA: SSP5-8.5 - historical

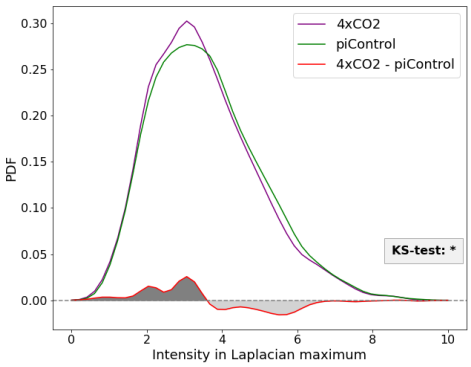

(b) NA: abrupt-4xCO2 - piControl

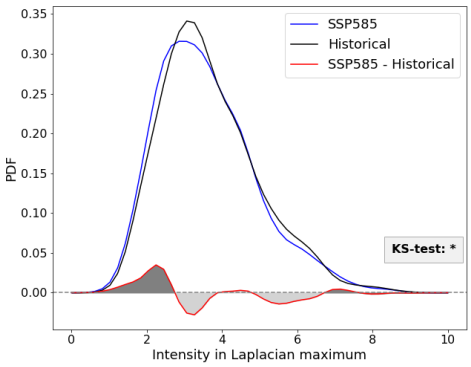

(c) Scan.: SSP5-8.5 - historical

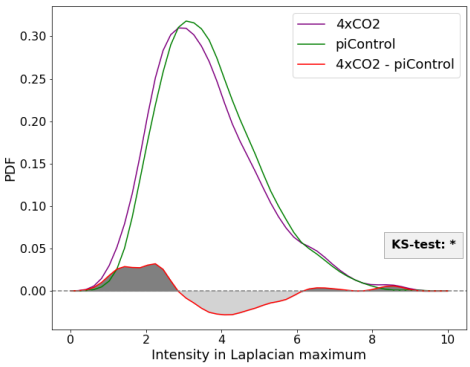

(d) Scan.: abrupt-4xCO2 - piControl

Figure 5.18: Probability density functions of intensity in maximum Laplacian. The top row represent NA, and the bottom row Scandinavia. Figure (a) and (c) represent the SSP5-8.5 - historical anomaly while (b) and (d) the represent the abrupt-4xCO2 - piControl. Calculated by selecting the point with maximum Laplacian in each track during DJF. PDFs of the maximum intensity are then calculated using the "gaussian_kde" module from scipy stats. The KS-test is performed with the "ks_2samp" module.

consistent with a negative surface temperature anomaly there. Contrarily, the scenarios show more precipitation around e.g. the east coast of North America, where we have the warm surface temperature anomalies. However, the precipitation anomalies varies largely from region to region, and other factors than temperature could influence the precipitation patterns.

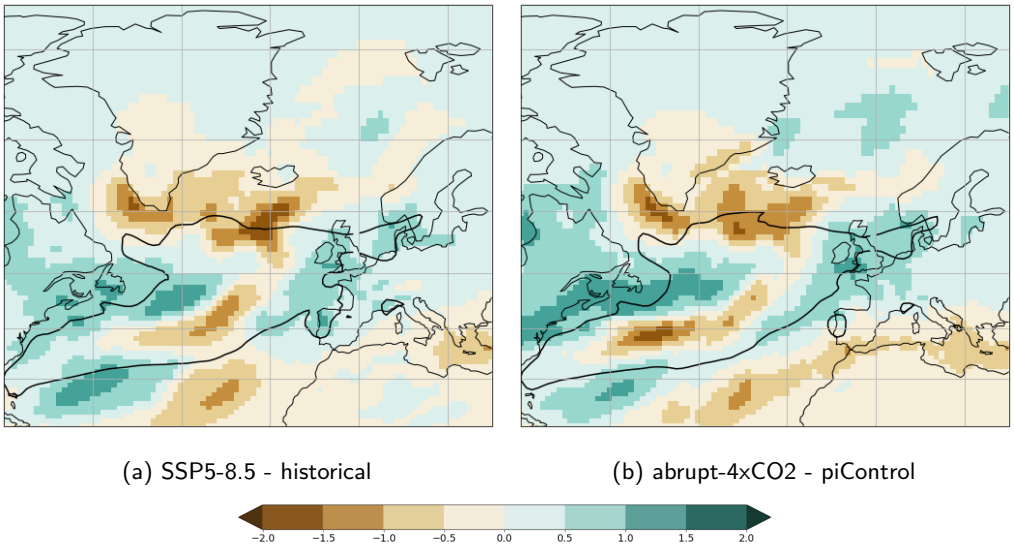

Figure 5.19: Mean DJF precipitation anomalies for (a) SSP5-8.5 - historical and (b) abrupt-4xCO2 - piControl. Total precipitation is composed of a sum of convective and large scale precipitation. The black contours represent the climatology of (a) the historical run and (b) the piControl, with the CI being 4 mm/day. Blue colors show larger amounts of precipitation and brown colors indicate less precipitation (unit: mm/day).

6 | Discussion

This chapter provides a discussion of the central findings in this thesis. Starting off, we give an evaluation of how well the chosen model, and models in general, perform in comparison to reanalysis products (6.1). Secondly, we investigate the mechanisms behind the changing cyclone characteristics (6.2). Finally, the choice of methods for this study and their limitations are discussed (6.3).

6.1 Model evaluation

From the results in Section 5.1 we see that the model agrees well with ERA-Interim when it comes to cyclone frequency, position and intensity. The model is thus suitable for use in this thesis. However, the model also shows some deviations from the reanalysis. This includes too high cyclone densities in Scandinavia, too much genesis south of Greenland and overall too few of the strongest storms.

In a GCM the cyclones result solely from numerical integration, while in a reanalysis, observational data are also incorporated. This makes GCMs well suited for determining the mechanisms that influence cyclones. CMIP6 models show an overall improvement compared to the earlier CMIP5 models (Priestley et al., 2020). AR6 points out several factors relevant for the uncertainties that still remain in the projections of cyclone characteristics. Such factors include horizontal resolution, resolution of the stratosphere and how changes in the Atlantic meridional overturning circulation (AMOC) are simulated (Douville et al.).

According to AR6, there is high confidence that the climate models with coarse resolution underestimate the intensity of cyclones, as we see a tendency to in Figure 5.3. Studies show that models with higher resolution show better performance by e.g. a better representation of the NA storm track tilt and the intensity of cyclones (Colle et al., 2013; Zappa et al., 2013a; Seiler et al., 2018). The bias in intensity is also linked to the inability of climate models to resolve diabatic processes well, especially related to the release of latent heat (Willison et al., 2013). Thus the models might not fully capture the future increase in latent heating, which lead to

cyclone intensification. This could explain why they concluded only medium confidence for a reduction in the frequency of the strongest storms (see Section 2.3.2) (Willison et al., 2015).

Other studies find that individual models capture the general characteristics of cyclones and storm tracks (Ulbrich et al., 2008; Catto et al., 2010). However, some models have deficiencies in capturing the location of storm tracks (Greeves et al., 2007; Catto et al., 2011). A longstanding issue with climate models, including the NorESM, is that they are not able to accurately reproduce the poleward tilt of the NA storm track (Seland et al., 2020). A too zonal or displaced southward NA storm track leads to too few and weak cyclones over the Norwegian Sea and too many cyclones in central Europe (Colle et al., 2013; Zappa et al., 2013a). A similar result is found in Figure 5.1 and Figure 5.2, where the model overestimates the genesis and density of storms in mid-latitudes. Tamarin-Brodsky and Kaspi (2017) found that increased latent heat release could make the cyclones propagate farther polewards. Since the zonal bias in the density in NA still remains, the inability of the CMIP6 models to capture the process of latent heat release could be the explanation here as well. In addition, Seland et al. (2020) find that in the models with increased resolution in the atmosphere and land components (e.g. NorESM2-MM), the bias of a too zonal storm track is reduced compared to models with lower resolution (e.g. NorESM2-LM). Higher horizontal resolution in future models could improve the representation of cyclone moist processes (e.g. Willison et al. (2013)), as well as air–sea coupling (e.g. Small et al. (2019)), and mean-flow interactions with orography (e.g. Pithan et al. (2016)). This would again lead to a better representation of the storm characteristics.

6.2 Changes in cyclone characteristics

We continue by studying how the cyclone characteristics change in the two different anomalies; abrupt-4xCO2 - piControl and SSP5-8.5 - historical. Overall, the anomalies are quite similar, but the abrupt-4xCO2 tends to be stronger. From now on, we refer to them both.

6.2.1 Position and number

For the point-density in the control run in Figure 5.4 we see that the NA storm track has a southwest-northeast tilt, and that the cyclones translate from the east coast of North America towards the Norwegian Sea. On the other hand, the geopotential height variance in Figure 5.5 shows a maximum in the variance over Newfoundland, rather than Greenland. Figure 5.5 is closer to the traditional expectation for the NA storm track than Figure 5.4. Brayshaw et al. (2009) find that the structure of the NA storm track is closely linked to the characteristics of the North American continent. The southwest–northeast tilt in the jet is found to be a result of the Rocky Mountains which deflects the westerly flow southwards. This leads to stronger

cyclone development along an axis similar to the North American continent's eastern coastline. In addition, the effect from the Gulf Stream and the NA drift must be taken into account. The storm track responses to these two effects tend to oppose one another. However, the combined pattern acts to enhance the tilt of the storm track (Brayshaw et al., 2011).

How the storm track will move due to climate change is not well understood. In Section 2.3.2 we mentioned several studies which find a poleward shift in the genesis latitude, such as Tamarin-Brodsky and Kaspi (2017) and Graff and LaCasce (2014). However, the shift is not as clear in the NH as in the SH and NP. Furthermore, regional responses are less clear than the zonal mean responses (Ulbrich et al., 2008). By using several experiments with fixed SSTs, Graff and LaCasce (2014) find that the in the run where the SSTs are increased by 2K polewards of 45 ° we get a relatively weak response, compared to the other experiments. In this run the Eady parameter anomalies are found to be weak and alternating between positive and negative values. This result is similar to what we find in Figure 5.7, where the Eady parameter anomalies only show clear changes in the SH. The run differs from the experiments in this study, but increasing the temperature by 2K polewards of 45 ° is comparable to the Arctic amplification we see in our own experiments.

The IPCC finds that the NA storm track is unlikely to have a simple poleward shift or to display any discernible changes (Douville et al.). This agrees well with the weak response we have for the Eady parameter. However, before we conclude that there are no discernible changes in the storm track position, a further investigation is of interest.

From Section 2.2 we know that the position of the storm track depends on processes that alter the meridional temperature gradients, which cyclones draw most of their energy from. Hence, we continue to investigate both surface- and air temperature anomalies. Global warming leads to several implications for the thermodynamics, and here we mention some: A warmer atmosphere yields increased saturation specific humidity via the Clausius-Clapeyron relation. This leads to moister low-level air and more latent heat release in tropical convection. As a result, we get a warm tropical upper troposphere relative to the surface, which also acts to raise the tropopause. The warm anomaly is seen in Figure 5.6 for both scenarios. Another result of global warming is Arctic amplification. Due to temperature- and surface albedo feedbacks, we get an enhanced warming in the Arctic relative to the global mean (Shaw et al., 2016). The Arctic amplification is seen in Figure 5.8. The first effect, tropical amplification, is found to increase the meridional temperature gradient in the upper-troposphere. This will increase the baroclinicity and shift the storms polewards. On the other hand, Arctic amplification acts to decrease the gradient in the lower-troposphere. The baroclinicity is thus decreased and the storms are shifted equatorward. In addition to the change in the meridional temperature gradient, we know from Equation 2.8 that the vertical potential temperature gradient also affects the baroclinicity. Hence, vertical

temperature gradients should also be taken into account when discussing the processes that alter the storm tracks. These examples illustrate the multiple opposing thermodynamic influences which makes future projections of storm tracks difficult (Shaw et al., 2016).

To understand the storm track responses to future climate change, we also have to study the local temperature anomalies. Local processes such as sea ice loss (Kvamstø et al., 2004; Bader et al., 2011; Seierstad and Bader, 2009) and changes in SSTs (Ciasto et al., 2016; Graff and LaCasce, 2012) are important for the response in some regions. Figure 5.9 shows the sea-ice loss anomalies. The temperature gradient and the static stability change as the sea-ice edge moves. Thus, the local response in baroclinicity due to sea-ice loss is a result of these two processes. An increase in the gradient could enhance the baroclinicity, while an increase in the stability will suppress it (Bader et al., 2011; Zahn and von Storch, 2010). As mentioned in Section 2.3.2, previous studies show opposing responses of storm tracks to a reduction in sea-ice cover. The Gulf stream, with its regions of strong surface baroclinicity, fuels the storm track growth. A variability in the SST gradients can move the overlying jet and storm track (Brayshaw et al., 2011). Global warming and the weakening of the AMOC are linked together and are expected to alter the SST gradients. How the SST gradients will respond is however not straightforward. The former effect will warm the SSTs along the Gulf stream, while the latter will reduce the transport of warm water polewards and cool the SSTs (Ciasto et al., 2016). The cold blob which complicates the surface temperature anomalies in Figure 5.8 is found to be a result of the weakening of the AMOC (Menary and Wood, 2018). In addition, the local land-sea contrast can influence the baroclinicity, for example along the North American eastern continental coastline (McDonald, 2011).

To see if there has been a shift in the storm track position, we must first understand where the cyclones typically form and where we have the strongest meridional temperature gradients. In Figure 5.10 we find that we have two main genesis areas; one off the east coast of North America and one south of Iceland. The main genesis regions are characterized by negative local meridional temperature gradients. The area in between the main genesis regions, close to the Newfoundland and Labrador coast, is however characterized by positive meridional temperature gradients. Brayshaw et al. (2009) link the high genesis density near the east coast to the strong surface temperature contrast across the eastern coastline. The strong contrast is found to be a result of the triangular shape of North America that sets up a cold pool of air in the northeast (Brayshaw et al., 2009). We also suggest the high genesis density near Iceland to be a result of strong local meridional temperature gradients. As mentioned, processes such as sea-ice and SSTs enhance the baroclinicity locally.

To understand the change in position, we study both the genesis density anomalies and the meridional temperature gradient anomalies in Figure 5.11. As explained in the results, we find

that the negative meridional temperature gradient anomaly in mid-latitudes are associated with more genesis there. The two main genesis areas are characterized by less genesis due to an increased gradient. The meridional temperature gradient anomalies are connected to the surface temperature changes seen in Figure 5.8. Thus, the cold blob affects the genesis.

Studying the PDFs of genesis latitude in Figure 5.12, we see that it is the Scandinavian storms that form further south in the scenarios. The NA storms do not show any significant changes in genesis latitude. We get a positive anomaly in the mid-latitudes (40-60 °N), and a negative anomaly elsewhere, as we also see in Figure 5.11. We conclude that the Scandinavian storms have a significant shift equatorward, but all together, there is no clear shift in the genesis latitude. We suggest that instead of a simple poleward shift (equatorward shift) due to the effect of tropical amplification (Arctic amplification), local processes such as sea-ice and SSTs affect the position (e.g. McDonald (2011); Bengtsson and Hodges (2006)). Thus, we get a tripole structure with more cyclones off Newfoundland, and less off the east coast of United States and Greenland. In addition, we speculate that the relatively modest storm track response reflects the partial cancelling of opposing tendencies (Butler et al., 2010; Catto et al., 2011).

When it comes to the number of cyclones, the IPCC projects an overall reduction by a few percent in the NH. However, low confidence is found in the regional projections (Douville et al.). Figure 5.13 and Table 5.1 also show the same response with a decrease of about 10 %. Some associate the decrease to the equatorward flank of the storm track, and link it to the Hadley cell expansion and the poleward shift in the genesis latitude of cyclones (Tamarin-Brodsky and Kaspi, 2017). However, in this study we do not find a clear poleward shift. Thus, another way to understand the reduction is by the decrease in the baroclinicity associated with a reduction in the pole-to-equator temperature gradient. This would reduce the available potential energy for the cyclones, and hinder their genesis (Bengtsson and Hodges, 2006). This result is also supported by McDonald (2011), Catto et al. (2011) and Bengtsson et al. (2009). Furthermore, we can expect more efficient poleward heat transport by cyclones due to the increase in water vapor. Therefore, the number of cyclones needed to move energy poleward decreases (Bengtsson and Hodges, 2006).

6.2.2 Displacement and intensity

In addition to investigating the change in position and number of cyclones, finding out how far they will travel and how intense they will be are also of interest.

In Figure 5.15 we find that the scenarios show an increase in the latitudinal displacement of cyclones. The most prominent results are however for the Scandinavian storms, where more storms travel around 10 to 40 ° polewards, and less storms travel southwards in the scenarios. Some find the increased latitudinal displacement to be a result of increased intensity. This is

explained by Kelvin's circulation theorem, which states that a stronger vortex could produce larger meridional displacements (Pedlosky, 1987). However, since the intensity decreases in this study, we do not find this explanation suitable. Tamarin-Brodsky and Kaspi (2017) link the increase in latitudinal displacement to the strengthening of the upper jet and the increased cyclone-related precipitation. The strengthening of the jet is also evident in Figure 5.14, where we have stronger wind speeds over the typical jet regions in the scenarios. Therefore we suggest the strengthened jet to be the explanation for the increased displacement in this study. In addition, we find that the Scandinavian storms form further south, while there was no significant change in the lysis latitudes. Altogether, we conclude that the latitudinal displacement increases in the scenarios.

An increased eastward advection is also found in Figure 5.16. As for the latitudinal displacement, the increase in longitudinal displacement is also found to be a result of the strengthened jet. Graff and LaCasce (2014) link the strengthening of the jet to stronger temperature gradients. Stronger gradients enhance the vertical shear and thus intensifies the jet. The PDFs are only significantly different for the NA storms. We suggest that this is a result of the location of the jet, advecting these storms farther eastwards than the Scandinavian storms.

There were no change in the cyclone lifetimes, and since we find that they travel farther, we conclude that they will also travel faster. Thus, the jet does not only lead the cyclones farther, but also increase their velocity.

The cyclone intensities in maximum Laplacian are seen in Figure 5.17. The strongest intensities are found in the yellow areas, which are located off the east coast of North America and the area to the northeast. When it comes to how the intensity will change in a future climate, previous studies show varying projections. Some find an increase in intensity (e.g. Lambert and Fyfe (2006); Mizuta et al. (2011)), while other find a decrease (e.g. Seiler and Zwiers (2016); Chang (2018)). Some also find relative little change (e.g. Bengtsson and Hodges (2006); Catto et al. (2011)). Overall, IPCC projects that changes in the dynamical intensity (e.g. wind speed) will be small and that the number of intense storms will decrease in NA (Lee et al.; Seneviratne et al.). Reduced low-level baroclinicity from SST and sea-ice changes is found to be the mechanism behind the decrease in the wind speeds and pressure deepening of cyclones. For comparison, in NP, intense cyclones are projected to increase due to the increased upper-level baroclinicity and poleward shift of the jet (Seiler and Zwiers, 2016).

Figure 5.18 shows the PDFs for the intensity in maximum Laplacian. For both regions and scenarios (except in NA for SSP5-8.5) we find that the number of weak storms will increase. In addition, the number of the intermediate storms will decrease and the number of strong storms show relatively little change. In addition to the reduced low-level baroclinicity, this can be linked to the increase in water vapor.

The projected increase in water vapor is likely to have competing effects. Latent heat gives energy to the individual cyclones (Shaw et al., 2016). However, the overall effect of moistening is to make the cyclones weaker by improving the efficiency of poleward heat transport, and hence reduce the baroclinicity (Schneider et al., 2010; Lucarini and Ragone, 2011).

Thus, regardless of how the intensity will change, there is high confidence that the number of cyclones associated with heavy precipitation will increase. This is due to the increase in atmospheric water vapor (Yettella and Kay, 2017; Hawcroft et al., 2018; Zappa et al., 2013b). Although changes in the intensity are found to be small, changes in the location can lead to large changes in the local extreme wind speeds (Chang, 2018; Yettella and Kay, 2017).

Figure 5.19 shows the precipitation anomalies during winter. We get less precipitation south of Iceland, consistent with a negative surface temperature anomaly there. Contrarily, the scenarios show more precipitation around e.g. the east coast of North America, where we have the warm surface temperature anomalies. More/less evaporation is found where the ocean is warmer/cooler, and hence we get more/less local precipitation (Stocker et al.). Thus, there are large regional differences in the anomalies (Hawcroft et al., 2018; Zappa et al., 2015). We would also expect the cyclones to affect the precipitation patterns, but we find no clear resemblance between this figure and Figure 5.11. Thus, we do not necessary have more precipitation where we have more cyclone genesis.

6.3 Limitations

Lack of agreement between studies on what changes we will have for the NA storm track is common. This is a result of several factors, such as opposing processes, the differences in models and scenarios being used and the different methods used for analysing the model outputs. We will now comment on our chosen methods.

First of all, the results in this thesis are based on a single model. In addition, we have only used one ensemble-member for all the experiments. The historical run has three members available while the other experiments (piControl, SSP5-8.5 and abrupt-4xCO2) only have one. In this study we use two scenarios, the SSP5-8.5 and abrupt-4xCO2. The strongest anomalies were typically found for the abrupt-4xCO2 scenario. However, using the abrupt-4xCO2 scenario as a basis for the future is not realistic. The scenario is simplified by a quadrupling of the atmospheric CO_2 concentration, leading to a rapid global warming. Yet, despite the simplicity, the scenario is convenient for studying how the climate system responds to global warming. In addition, natural interannual variability obscures the results, and the calculated anomalies can thus be misleading.

In addition to only using one model, we have used a single tracking scheme which captures

cyclones in the Lagrangian framework. We could also have used the Eulerian framework as we did in Figure 5.5 to a greater extent. However, the decision fell on the Lagrangian due to its capability of following the cyclones, and being able to find more cyclone characteristics. In addition to the choice in approach, the identification variable will also affect the output. In this study, the MSLP is used as the identification variable. A limitation of using the MSLP is that it is influenced by strong background flows. For example can weak cyclones be masked by the background flow until they have developed. The same limitation is found for the 500-hPa geopotential. The vorticity focuses on smaller spatial scales and is found to be less influenced by the background flow. It can therefore identify cyclones earlier in their life cycle. However, smoothing or reduction in resolution are often necessary since the field can be very noisy (Hoskins and Hodges, 2002). We did not use a topographic filter in the tracking algorithm, thus the orography could influence the results. This is likely one of the reasons for the high point-density of cyclones west of Iceland. Applying a topographic filter in the methods could smooth the output.

The Eady parameter in Figure 5.7 shows unrealistically high values for the climatologies and anomalies, compared to Figure 2.6 from Yin (2005). Using another expression for the Eady parameter such as Equation 2.6, might simplify the calculations, help find the potential error and reduce the limitations.

When it comes to the scope of the thesis, several choices were made. The focus is on the NA storm track during the winter months (DJF). We defined two main regions where the cyclones have to travel to be called NA- or Scandinavian storms. These regions could be defined in several ways. In addition, the cyclones that lived less than two days were filtered out. The temporal resolution of 6 hours is also important. A lower temporal resolution implies a reduced number of cyclone tracks, and it can mainly affect the short-lived, weaker cyclones (Ulbrich et al., 2009). Such decisions influence the results, and will vary from study to study.

7 | Conclusion

This final section concludes the thesis. It contains a summary of the study and the main findings (7.1), together with a section on further work (7.2).

7.1 Summary and main findings

The low confidence in projected changes for the NA storm track motivated this study. The NA winter cyclone characteristics were determined using an objective Lagrangian tracking algorithm, applied to the MSLP. For the first part, a comparison of the statistic from NorESM2 with the statistics from ERA-Interim was made, and the extent of the mismatch was assessed. For the second part, we study how the characteristics of cyclones are changing by comparing the models control runs with the abrupt-4xCO2 and SSP5-8.5 scenarios.

A good agreement is found between the NorESM2 and ERA-Interim. Nevertheless, the model underestimates the number of strong storms and overestimates both the genesis south of Greenland and the cyclone densities in Scandinavia. This is suggested to be a result of a too coarse horizontal resolution, and the inability of the climate model to resolve diabatic processes, such as the ones related to latent heat release.

When it comes to the changes in cyclone characteristics, several results are found. The zonally averaged Eady parameter did not show any clear shift in the genesis latitude. However, we found a tripole structure with more genesis in mid-latitudes (40-60 °N), and less north and south of this. This is found to be a result of changes in the meridional temperature gradient anomaly in the mid-latitudes, which is linked to processes such as sea-ice and SSTs. The negative gradient is found to enhance the baroclinicity locally. The relatively modest storm track response in genesis is suggested to be a result of the partial cancelling of opposing tendencies due to changes in static stability and and surface baroclinicity.

An overall reduction in the number of storms is found in both areas and scenarios. The reduction is found to be a result of the decrease in the pole-to-equator temperature gradient which reduces the available potential energy for the cyclones. Furthermore, with an increase in

water vapor, the poleward heat transport by cyclones becomes more efficient. Thus, less storms are necessary in a future climate.

We find that the storms translate farther, both polewards and eastwards. This is found to be a result of a strengthening of the upper jet due to increased temperature gradients, and increased cyclone-related precipitation. We found no change in the lifetimes of cyclones, and since we know that they travel farther, we conclude that the jet also makes the cyclones travel faster.

The number of weak storms are expected to increase. Even if more latent heating is expected in the future, the overall effect of increased moisture content is to make the storms weaker by increasing the efficiency of poleward heat transport, and thereby reducing the baroclinicity. Thus, we can get more precipitation despite no increase in the intensity of the cyclones. The precipitation anomalies varies from region to region, as the pattern closely resembles surface temperature.

7.2 Future work

Time limitations restrict the extent of the research in a Master's thesis. Nevertheless, several ideas for further work have emerged. Here, we present some of these ideas.

Since only one model was applied, an intercomparison with other models or versions would be of interest. It would also be interesting to check if the model performs better with increased horizontal resolution. We could then consider whether increased horizontal resolution in the atmosphere- and ocean components of the model improves the model's ability to simulate cyclone characteristics. This could be done by using the CMIP6 historical experiments carried out with low- and medium-resolution versions of NorESM2.

In addition, since only one tracking algorithm is used, both a comparison with other Lagrangian approaches, but also Eulerian approaches would be useful. We could for example repeat the Lagrangian tracking but with a topographic filter, and compare the results to the current ones. If we were to apply an Eulerian approach, studying the geopotential height field in more detail would be of interest. In this study, the geopotential height variance has been used to study the storm activity. However, we only studied the control runs, not the scenarios. By including the scenarios and finding anomalies, we could get more information on how the storm characteristics will change.

In this study, the variable used for identifying and tracking cyclones is the MSLP. Since the central pressure depends on the background MSLP, studying the intensity could be problematic (Seneviratne et al.). Therefore, the Laplacian of the pressure is also used, yielding different results. To get even more perspective on how we expect the intensity of cyclones to change, other measures for the intensity such as cyclone related wind- and precipitation could be used.

With that in mind, we could study the link between precipitation and cyclones in more detail, by for example looking at the latent heat release.

From previous studies such as Graff and LaCasce (2012), we know that SSTs could influence the position of the storm track. Connecting the changes in surface temperatures in this study, to the changes in the SSTs are of interest to see how it is all related. Here we have personal communication with Gaurav Madan who has an article in progress about this topic.

Appendices

A | Additional figures

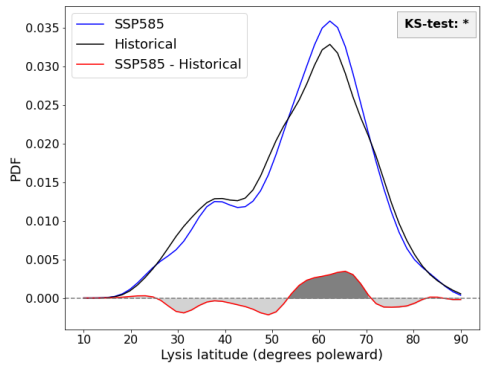

(a) NA: SSP5-8.5 - historical

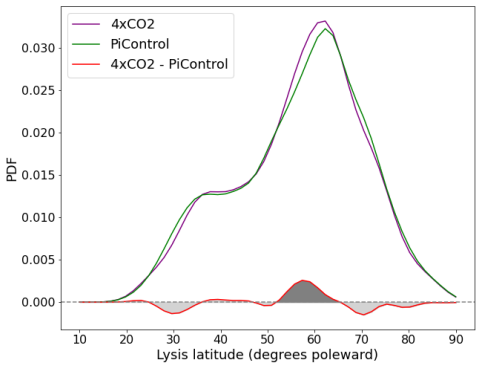

(b) NA: abrupt-4xCO2 - piControl

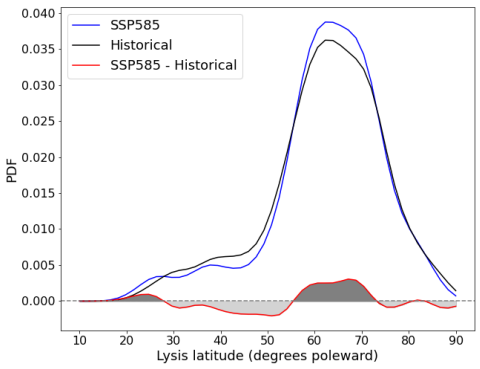

(c) Scan.: SSP5-8.5 - historical

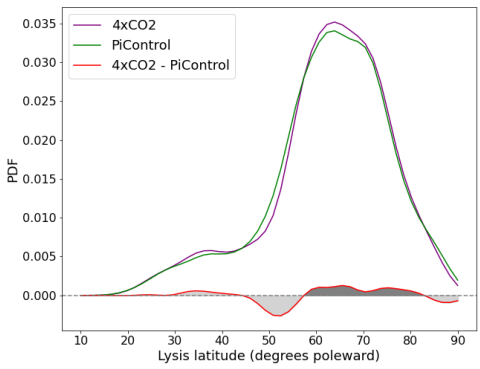

(d) Scan.: abrupt-4xCO2 - piControl

Figure A.1: Probability density functions of lysis latitude. The top row represent NA, and the bottom row Scandinavia. Figure (a) and (c) represent the SSP5-8.5 - historical anomaly while (b) and (d) the represent the abrupt-4xCO2 - piControl. Calculated by choosing the last point in each track during DJF, and selecting the corresponding latitudes. PDFs of the lysis latitudes are then calculated using the "gaussian_kde" module from scipy stats. The KS-test is performed with the "ks_2samp" module.

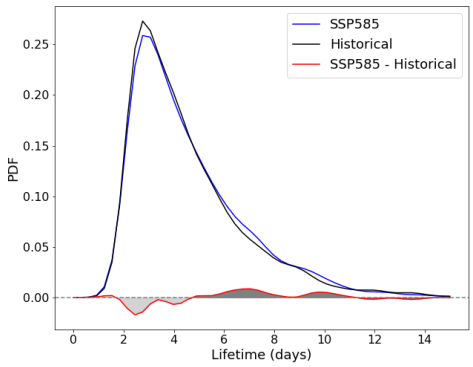

(a) NA: SSP5-8.5 - historical

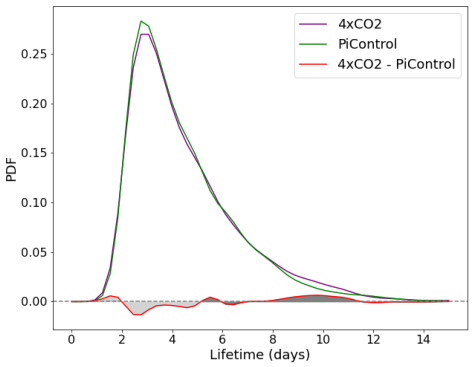

(b) NA: abrupt-4xCO2 - piControl

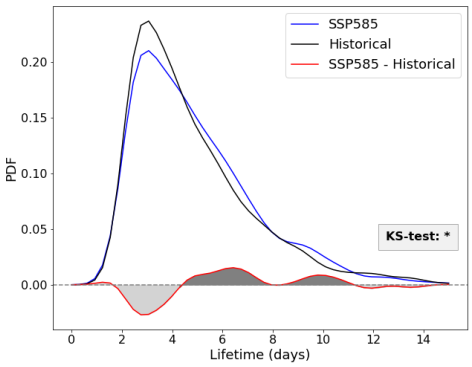

(c) Scandinavia: SSP5-8.5 - historical

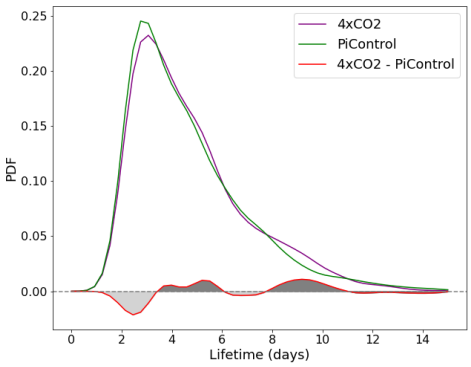

(d) Scandinavia: abrupt-4xCO2 - piControl

Figure A.2: Probability density functions of lifetimes. The top row represent NA, and the bottom row Scandinavia. Figure (a) and (c) represent the SSP5-8.5 - historical anomaly while (b) and (d) the represent the abrupt-4xCO2 - piControl. An array with the lifetimes (in days) for each cyclone during DJF is created. PDFs of the lifetimes are then calculated using the "gaussian_kde" module from scipy stats. The KS-test is performed with the "ks_2samp" module.

B | Variables

Table B.1: The variables used for the CMIP6 framework.

Variable	Long name	Table ID
psl	Sea level pressure	6hrPlev
ts	Surface temperature	Amon
ta	Air temperature	Amon
ua	Eastward wind	Amon
va	Northward wind	Amon
pr	Precipitation	Amon
zg	Geopotential height	Amon
siconc	Sea ice area percentage (ocean grid)	SImon

C | Acronyms

AMOC Atlantic Meridional Overturning Circulation

AR Assessment Report

BLOM Bergen Layered Ocean Model

BP Bandpass

CAM Community Atmosphere Model

CESM Community Earth System Model

CESM-LE Community Earth System Model Large Ensemble

CMIP Coupled Model Intercomparison Project

DA Data Assimilation

DJF December, January and February

ECS Equilibrium Climate Sensitivity

EKE Eddy Kinetic Energy

ERA-Interim ECMWF Reanalysis-Interim

ESM Earth System Model

GCM General Circulation Model

IPCC Intergovernmental Panel on Climate Change

JJA June, July and August

MICOM Miami Isopycnic Coordinate Ocean Model

MSLP Mean Sea Level Pressure

NA North Atlantic

NAO North Atlantic Oscillation

NCAR National Center for Atmospheric Research

NCC Norwegian Climate Center

NH Northern Hemisphere

NorESM Norwegian Earth System Model

NP North Pacific

PAMIP Polar Amplification Model Intercomparison Project

RCP Representative Concentration Pathway

ScenarioMIP Scenario Model Intercomparison Project

SH Southern Hemisphere

SLP Sea Level Pressure

SSP Shared Socioeconomic Pathway

SST Sea Surface Temperature

4D-Var 4-Dimensional Variational Analysis

Bibliography

J. Bader, M. D. Mesquita, K. I. Hodges, N. Keenlyside, S. Østerhus, and M. Miles. A review on northern hemisphere sea-ice, storminess and the north atlantic oscillation: Observations and projected changes. *Atmospheric Research*, 101(4):809–834, 2011.

R. Benestad and D. Chen. The use of a calculus-based cyclone identification method for generating storm statistics. *Tellus A*, 56(4):473–486, 2006.

L. Bengtsson and K. Hodges. Storm tracks and climate change. *Journal of climate*, 19(1), 2006.

L. Bengtsson, K. I. Hodges, and N. Keenlyside. Will extratropical storms intensify in a warmer climate? *Journal of Climate*, 22(9):2276–2301, 2009.

P. Berrisford, D. Dee, P. Poli, R. Brugge, K. Fielding, M. Fuentes, P. Kallberg, S. Kobayashi, S. Uppala, and A. Simmons. The era-interim archive, version 2.0. *ERA report series. 1. Technical Report*, 2011.

M. Blackmon. A Climatological Spectral Study of the 500 mb Geopotential Height of the Northern Hemisphere. *Journal of the Atmospheric Sciences*, 33(8):1607–1623, 08 1976.

M. Blackmon et al. An Observational Study of the Northern Hemisphere Wintertime Circulation. *Journal of the Atmospheric Sciences*, 34(7):1040–1053, 07 1977.

J. F. Booth, Y.-O. Kwon, S. Ko, R. J. Small, and R. Msadek. Spatial patterns and intensity of the surface storm tracks in cmip5 models. *Journal of Climate*, 30(13):4965–4981, 2017.

D. Brayshaw, B. Hoskins, and M. Blackburn. The basic ingredients of the north atlantic storm track. part i: Land–sea contrast and orography. *Journal of the Atmospheric Sciences*, 66: 2539–2558, 09 2009.

D. J. Brayshaw, B. Hoskins, and M. Blackburn. The basic ingredients of the north atlantic storm track. part ii: Sea surface temperatures. *Journal of the Atmospheric Sciences*, 68(8): 1784–1805, 2011.

A. H. Butler, D. W. Thompson, and R. Heikes. The steady-state atmospheric circulation response to climate change–like thermal forcings in a simple general circulation model. *Journal of Climate*, 23(13):3474–3496, 2010.

J. L. Catto, L. C. Shaffrey, and K. I. Hodges. Can climate models capture the structure of extratropical cyclones? *Journal of Climate*, 23(7):1621–1635, 2010.

J. L. Catto, L. C. Shaffrey, and K. I. Hodges. Northern hemisphere extratropical cyclones in a warming climate in the higem high-resolution climate model. *Journal of Climate*, 24(20): 5336–5352, 2011.

E. K. Chang and A. M. Yau. Northern hemisphere winter storm track trends since 1959 derived from multiple reanalysis datasets. *Climate Dynamics*, 47(5):1435–1454, 2016.

E. K. Chang, S. Lee, and K. L. Swanson. Storm track dynamics. *Journal of climate*, 15(16): 2163–2183, 2002.

E. K.-M. Chang. Cmip5 projected change in northern hemisphere winter cyclones with associated extreme winds. *Journal of Climate*, 31(16):6527–6542, 2018.

J. Charney. The dynamics of long waves in a baroclinic westerly current. *Journal of Atmospheric Sciences*, 4(5):136–162, 1947.

L. M. Ciasto, C. Li, J. J. Wettstein, and N. G. Kvamstø. North atlantic storm-track sensitivity to projected sea surface temperature: Local versus remote influences. *Journal of Climate*, 29 (19):6973–6991, 2016.

B. A. Colle, Z. Zhang, K. A. Lombardo, E. Chang, P. Liu, and M. Zhang. Historical evaluation and future prediction of eastern north american and western atlantic extratropical cyclones in the cmip5 models during the cool season. *Journal of Climate*, 26(18):6882–6903, 2013.

D. P. Dee, S. M. Uppala, A. Simmons, P. Berrisford, P. Poli, S. Kobayashi, U. Andrae, M. Balmaseda, G. Balsamo, d. P. Bauer, et al. The era-interim reanalysis: Configuration and performance of the data assimilation system. *Quarterly Journal of the royal meteorological society*, 137(656):553–597, 2011.

H. Douville, K. Raghavan, J. Renwick, R. Allan, P. Arias, M. Barlow, R. Cerezo-Mota, A. Cherchi, T. Gan, J. Gergisa, D. Jiang, A. Khan, W. P. Mba, D. Rosenfeld, J. Tierney, and O. Zolina:. 2021: Water Cycle Changes. In Climate Change 2021: The Physical Science Basis. Contribution of Working Group I to the Sixth Assessment Report of the Intergovernmental Panel on Climate Change [Masson-Delmotte, V., P. Zhai, A. Pirani, S.L. Connors, C. Péan, S. Berger, N.

Caud, Y. Chen, L. Goldfarb, M.I. Gomis, M. Huang, K. Leitzell, E. Lonnoy, J.B.R. Matthews, T.K. Maycock, T. Waterfield, O. Yelekçi, R. Yu, and B. Zhou (eds.)]. Cambridge University Press. In press.

E. T. Eady. Long waves and cyclone waves. *Tellus*, 1(3):33–52, 1949.

V. Eyring, S. Bony, G. A. Meehl, C. A. Senior, B. Stevens, R. J. Stouffer, and K. E. Taylor. Overview of the coupled model intercomparison project phase 6 (cmip6) experimental design and organization. *Geoscientific Model Development*, 9(5):1937–1958, 2016.

L. Graff and J. LaCasce. Changes in cyclone characteristics in response to modified ssts. *Journal of climate*, 27(11):4273–4295, 2014.

L. S. Graff and J. LaCasce. Changes in the extratropical storm tracks in response to changes in sst in an agcm. *Journal of Climate*, 25(6):1854–1870, 2012.

C. Greeves, V. Pope, R. Stratton, and G. Martin. Representation of northern hemisphere winter storm tracks in climate models. *Climate dynamics*, 28(7-8):683–702, 2007.

S. Gulev, P. Thorne, J. Ahn, F. Dentener, C. Domingues, S. Gerland, D. Gong, D. Kaufman, H. Nnamchi, J. Quaas, J. Rivera, S. Sathyendranath, S. Smith, B. Trewin, K. von Schuckmann, and R. Vose:. 2021: Changing State of the Climate System. In Climate Change 2021: The Physical Science Basis. Contribution of Working Group I to the Sixth Assessment Report of the Intergovernmental Panel on Climate Change [MassonDelmotte, V., P. Zhai, A. Pirani, S.L. Connors, C. Péan, S. Berger, N. Caud, Y. Chen, L. Goldfarb, M.I. Gomis, M. Huang, K. Leitzell, E. Lonnoy, J.B.R. Matthews, T.K. Maycock, T. Waterfield, O. Yelekçi, R. Yu, and B. Zhou (eds.)]. Cambridge University Press. In press.

K. Harstveit. Nyttårsorkanen (1992), 2019. URL `https://snl.no/Nyttårsorkanen_(1992)`.

M. Hawcroft, E. Walsh, K. Hodges, and G. Zappa. Significantly increased extreme precipitation expected in europe and north america from extratropical cyclones. *Environmental research letters*, 13(12):124006, 2018.

R. Hinman. *Eclectic physical geography.* American Book Company, 1888.

K. I. Hodges. A general method for tracking analysis and its application to meteorological data. *Monthly Weather Review*, 122(11):2573–2586, 1994.

J. Holton. *An Introduction to Dynamical Meteorology.* International Geophysics Series. Elsevier, London, 4 edition, 2004.

B. J. Hoskins and K. I. Hodges. New Perspectives on the Northern Hemisphere Winter Storm Tracks. *Journal of the Atmospheric Sciences*, 59(6):1041–1061, 03 2002.

B. J. Hoskins and P. J. Valdes. On the existence of storm-tracks. *Journal of Atmospheric Sciences*, 47(15):1854–1864, 1990.

IPCC. 2021: Summary for Policymakers. In: Climate Change 2021: The Physical Science Basis. Contribution of Working Group I to the Sixth Assessment Report of the Intergovernmental Panel on Climate Change [MassonDelmotte, V., P. Zhai, A. Pirani, S.L. Connors, C. Péan, S. Berger, N. Caud, Y. Chen, L. Goldfarb, M.I. Gomis, M. Huang, K. Leitzell, E. Lonnoy, J.B.R. Matthews, T.K. Maycock, T. Waterfield, O. Yelekçi, R. Yu, and B. Zhou (eds.)]. Cambridge University Press, a. In press.

IPCC. 2021: Annex VII: Glossary [Matthews, J.B.R. and V. Möller and R. van Diemen and J.S. Fuglestvedt and V. MassonDelmotte and C. Méndez and S. Semenov and A. Reisinger (eds.)]. In Climate Change 2021: The Physical Science Basis. Contribution of Working Group I to the Sixth Assessment Report of the Intergovernmental Panel on Climate Change [Masson-Delmotte, V., P. Zhai, A. Pirani, S.L. Connors, C. Péan, S. Berger, N. Caud, Y. Chen, L. Goldfarb, M.I. Gomis, M. Huang, K. Leitzell, E. Lonnoy, J.B.R. Matthews, T.K. Maycock, T. Waterfield, O. Yelekçi, R. Yu, and B. Zhou (eds.)]. Cambridge University Press, b. In press.

R. A. Johnson and G. K. Bhattacharyya. *Statistics: principles and methods*. John Wiley & Sons, 2019.

E. M. Knudsen and J. E. Walsh. Northern hemisphere storminess in the norwegian earth system model (noresm1-m). *Geoscientific Model Development*, 9(7):2335–2355, 2016.

N. G. Kvamstø, P. Skeie, and D. B. Stephenson. Impact of labrador sea-ice extent on the north atlantic oscillation. *International Journal of Climatology: A Journal of the Royal Meteorological Society*, 24(5):603–612, 2004.

J. H. LaCasce. *Atmosphere-Ocean Dynamics*. Dept. of Geosciences, University of Oslo, 2020.

S. J. Lambert and J. C. Fyfe. Changes in winter cyclone frequencies and strengths simulated in enhanced greenhouse warming experiments: results from the models participating in the ipcc diagnostic exercise. *Climate Dynamics*, 26(7-8):713–728, 2006.

J.-Y. Lee, J. Marotzke, G. Bala, L. Cao, S. Corti, J. Dunne, F. Engelbrecht, E. Fischer, J. Fyfe, C. Jones, A. Maycock, J. Mutemi, O. Ndiaye, S. Panickal, and T. Zhou:. 2021, Future Global Climate: Scenario-Based Projections and Near-Term Information. In Climate Change 2021: The Physical Science Basis. Contribution of Working Group I to the Sixth Assessment Report

of the Intergovernmental Panel on Climate Change [Masson-Delmotte, V., P. Zhai, A. Pirani, S.L. Connors, C. Péan, S. Berger, N. Caud, Y. Chen, L. Goldfarb, M.I. Gomis, M. Huang, K. Leitzell, E. Lonnoy, J.B.R. Matthews, T.K. Maycock, T. Waterfield, O. Yelekçi, R. Yu, and B. Zhou (eds.)] . Cambridge University Press. In press.

R. Lindzen and B. Farrell. A simple approximate result for the maximum growth rate of baroclinic instabilities. *Journal of the atmospheric sciences*, 37(7):1648–1654, 1980.

J. Lu, G. Chen, and D. M. Frierson. The position of the midlatitude storm track and eddy-driven westerlies in aquaplanet agcms. *Journal of Atmospheric Sciences*, 67(12):3984–4000, 2010.

V. Lucarini and F. Ragone. Energetics of climate models: Net energy balance and meridional enthalpy transport. *Reviews of Geophysics*, 49(1), 2011.

G. Magnusdottir, C. Deser, and R. Saravanan. The effects of north atlantic sst and sea ice anomalies on the winter circulation in ccm3. part i: Main features and storm track characteristics of the response. *Journal of Climate*, 17(5):857–876, 2004.

J. E. Martin. *Mid-latitude atmospheric dynamics: a first course*. John Wiley & Sons, 2006.

C. Mbengue and T. Schneider. Storm track shifts under climate change: What can be learned from large-scale dry dynamics. *Journal of Climate*, 26(24):9923–9930, 2013.

R. E. McDonald. Understanding the impact of climate change on northern hemisphere extratropical cyclones. *Climate Dynamics*, 37(7-8):1399–1425, 2011.

M. B. Menary and R. A. Wood. An anatomy of the projected north atlantic warming hole in cmip5 models. *Climate Dynamics*, 50(7):3063–3080, 2018.

R. Mizuta, M. Matsueda, H. Endo, and S. Yukimoto. Future change in extratropical cyclones associated with change in the upper troposphere. *Journal of Climate*, 24(24):6456–6470, 2011.

R. H. Moss, J. A. Edmonds, K. A. Hibbard, M. R. Manning, S. K. Rose, D. P. Van Vuuren, T. R. Carter, S. Emori, M. Kainuma, T. Kram, et al. The next generation of scenarios for climate change research and assessment. *Nature*, 463(7282):747–756, 2010.

R. J. Murray and I. Simmonds. A numerical scheme for tracking cyclone centres from digital data. part i: Development and operation of the scheme. *Australian Meteorological Magazine*, 39(3):155–166, 1991a.

R. J. Murray and I. Simmonds. A numerical scheme for tracking cyclone centres from digital data. part ii: Application to january and july general circulation model simulations. *Australian Meteorological Magazine*, 39(3):167–180, 1991b.

U. Neu, M. G. Akperov, N. Bellenbaum, R. Benestad, R. Blender, R. Caballero, A. Cocozza, H. F. Dacre, Y. Feng, K. Fraedrich, et al. Imilast: A community effort to intercompare extratropical cyclone detection and tracking algorithms. *Bulletin of the American Meteorological Society*, 94(4):529–547, 2013.

B. C. O'Neill, C. Tebaldi, D. P. v. Vuuren, V. Eyring, P. Friedlingstein, G. Hurtt, R. Knutti, E. Kriegler, J.-F. Lamarque, J. Lowe, et al. The scenario model intercomparison project (scenariomip) for cmip6. *Geoscientific Model Development*, 9(9):3461–3482, 2016.

J. Pedlosky. *Geophysical fluid dynamics*, volume 710. Springer, 1987.

N. A. Phillips. Energy transformations and meridional circulations associated with simple baroclinic waves in a two-level, quasi-geostrophic model. *Tellus*, 6(3):274–286, 1954.

J. G. Pinto, T. Spangehl, U. Ulbrich, and P. Speth. Sensitivities of a cyclone detection and tracking algorithm: individual tracks and climatology. *Meteorologische Zeitschrift*, 14(6):823–838, 2005.

F. Pithan, T. G. Shepherd, G. Zappa, and I. Sandu. Climate model biases in jet streams, blocking and storm tracks resulting from missing orographic drag. *Geophysical Research Letters*, 43(13): 7231–7240, 2016.

M. D. Priestley, D. Ackerley, J. L. Catto, K. I. Hodges, R. E. McDonald, and R. W. Lee. An overview of the extratropical storm tracks in cmip6 historical simulations. *Journal of Climate*, 33(15):6315–6343, 2020.

C. H. Reitan. Frequencies of Cyclones and Cyclogenesis for North America, 1951–1970. *Monthly Weather Review*, 102(12):861–868, 12 1974.

T. Sampe, H. Nakamura, A. Goto, and W. Ohfuchi. Significance of a midlatitude sst frontal zone in the formation of a storm track and an eddy-driven westerly jet. *Journal of Climate*, 23(7):1793–1814, 2010.

T. Schneider, P. A. O'Gorman, and X. J. Levine. Water vapor and the dynamics of climate changes. *Reviews of Geophysics*, 48(3), 2010.

D. Schultz et al. Extratropical cyclones: A century of research on meteorology's centerpiece. *Meteorological monographs*, 59:16–1, 2019.

I. A. Seierstad and J. Bader. Impact of a projected future arctic sea ice reduction on extratropical storminess and the nao. *Climate dynamics*, 33(7-8):937, 2009.

C. Seiler and F. W. Zwiers. How will climate change affect explosive cyclones in the extratropics of the northern hemisphere? *Climate Dynamics*, 46(11):3633–3644, 2016.

C. Seiler, F. Zwiers, K. I. Hodges, and J. Scinocca. How does dynamical downscaling affect model biases and future projections of explosive extratropical cyclones along north america's atlantic coast? *Climate dynamics*, 50(1):677–692, 2018.

Ø. Seland, M. Bentsen, D. Olivié, T. Toniazzo, A. Gjermundsen, L. S. Graff, J. B. Debernard, A. K. Gupta, Y.-C. He, A. Kirkevåg, et al. Overview of the norwegian earth system model (noresm2) and key climate response of cmip6 deck, historical, and scenario simulations. *Geoscientific Model Development*, 13(12):6165–6200, 2020.

S. Seneviratne, X. Zhang, M. Adnan, W. Badi, C. Dereczynski, A. D. Luca, S. Ghosh, I. Iskandar, J. Kossin, S. Lewis, F. Otto, I. Pinto, M. Satoh, S. Vicente-Serrano, M. Wehner, and . B. Zhou. 2021: Weather and Climate Extreme Events in a Changing Climate. In Climate Change 2021: The Physical Science Basis. Contribution of Working Group I to the Sixth Assessment Report of the Intergovernmental Panel on Climate Change [MassonDelmotte, V., P. Zhai, A. Pirani, S.L. Connors, C. Péan, S. Berger, N. Caud, Y. Chen, L. Goldfarb, M.I. Gomis, M. Huang, K. Leitzell, E. Lonnoy, J.B.R. Matthews, T.K. Maycock, T. Waterfield, O. Yelekçi, R. Yu, and B. Zhou (eds.)]. Cambridge University Press. In press.

M. C. Serreze. Climatological aspects of cyclone development and decay in the arctic. *Atmosphere-Ocean*, 33(1):1–23, 1995.

T. Shaw, M. Baldwin, E. A. Barnes, et al. Storm track processes and the opposing influences of climate change. *Nature Geoscience*, 9(9), 2016.

T. A. Shaw and A. Voigt. What can moist thermodynamics tell us about circulation shifts in response to uniform warming? *Geophysical Research Letters*, 43(9):4566–4575, 2016.

M. R. Sinclair. An Objective Cyclone Climatology for the Southern Hemisphere. *Monthly Weather Review*, 122(10):2239–2256, 10 1994.

R. J. Small, R. Msadek, Y.-O. Kwon, J. F. Booth, and C. Zarzycki. Atmosphere surface storm track response to resolved ocean mesoscale in two sets of global climate model experiments. *Climate Dynamics*, 52(3):2067–2089, 2019.

D. M. Smith, J. A. Screen, C. Deser, J. Cohen, J. C. Fyfe, J. García-Serrano, T. Jung, V. Kattsov, D. Matei, R. Msadek, et al. The polar amplification model intercomparison project (pamip) contribution to cmip6: investigating the causes and consequences of polar amplification. *Geoscientific Model Development*, 12(3):1139–1164, 2019.

T. Stocker, G.-K. P. D. Qin, L. Alexander, S. Allen, N. Bindoff, F.-M. Bréon, J. Church, U. Cubasch, S. Emori, P. Forster, P. Friedlingstein, N. Gillett, J. Gregory, D. Hartmann, E. Jansen, B. Kirtman, R. Knutti, K. K. Kumar, P. Lemke, J. Marotzke, V. Masson-Delmotte, G. Meehl, I. Mokhov, S. Piao, V. Ramaswamy, D. Randall, M. Rhein, M. Rojas, C. Sabine, D. Shindell, L. Talley, D. Vaughan, and S.-P. Xie. 2013: Technical Summary. In: Climate Change 2013: The Physical Science Basis. Contribution of Working Group I to the Fifth Assessment Report of the Intergovernmental Panel on Climate Change [Stocker, T.F., D. Qin, G.-K. Plattner, M. Tignor, S.K. Allen, J. Boschung, A. Nauels, Y. Xia, V. Bex and P.M. Midgley (eds.)]. Cambridge University Press, Cambridge, United Kingdom and New York, NY, USA.

T. Tamarin-Brodsky and Y. Kaspi. Enhanced poleward propagation of storms under climate change. *Nature geoscience*, 10(12):908–913, 2017.

N. Tilinina, S. K. Gulev, I. Rudeva, and P. Koltermann. Comparing cyclone life cycle characteristics and their interannual variability in different reanalyses. *Journal of Climate*, 26(17): 6419–6438, 2013.

U. Ulbrich, J. G. Pinto, H. Kupfer, G. Leckebusch, T. Spangehl, and M. Reyers. Changing northern hemisphere storm tracks in an ensemble of ipcc climate change simulations. *Journal of Climate*, 21(8):1669–1679, 2008.

U. Ulbrich, G. Leckebusch, and J. G. Pinto. Extra-tropical cyclones in the present and future climate: a review. *Theoretical and Applied Climatology*, 96(1-2):117–131, 2009.

P. Virtanen, R. Gommers, T. E. Oliphant, M. Haberland, T. Reddy, D. Cournapeau, E. Burovski, P. Peterson, W. Weckesser, J. Bright, S. J. van der Walt, M. Brett, J. Wilson, K. J. Millman, N. Mayorov, A. R. J. Nelson, E. Jones, R. Kern, E. Larson, C. J. Carey, İ. Polat, Y. Feng, E. W. Moore, J. VanderPlas, D. Laxalde, J. Perktold, R. Cimrman, I. Henriksen, E. A. Quintero, C. R. Harris, A. M. Archibald, A. H. Ribeiro, F. Pedregosa, P. van Mulbregt, and SciPy 1.0 Contributors. SciPy 1.0: Fundamental Algorithms for Scientific Computing in Python. *Nature Methods*, 17:261–272, 2020.

E. Walker, D. Mitchell, and W. Seviour. The numerous approaches to tracking extratropical cyclones and the challenges they present. *Weather*, 75(11):336–341, 2020.

J. Willison, W. A. Robinson, and G. M. Lackmann. The importance of resolving mesoscale latent heating in the north atlantic storm track. *Journal of the Atmospheric Sciences*, 70(7): 2234–2250, 2013.

J. Willison, W. A. Robinson, and G. M. Lackmann. North atlantic storm-track sensitivity to warming increases with model resolution. *Journal of Climate*, 28(11):4513–4524, 2015.

V. Yettella and J. E. Kay. How will precipitation change in extratropical cyclones as the planet warms? insights from a large initial condition climate model ensemble. *Climate Dynamics*, 49 (5):1765–1781, 2017.

J. Yin. A consistent poleward shift of the storm tracks in simulations of 21st century climate. *Geophysical Research Letters*, 32(1), 2005.

M. Zahn and H. von Storch. Decreased frequency of north atlantic polar lows associated with future climate warming. *Nature*, 467(7313):309–312, 2010.

G. Zappa, L. C. Shaffrey, and K. I. Hodges. The ability of cmip5 models to simulate north atlantic extratropical cyclones. *Journal of Climate*, 26(15):5379–5396, 2013a.

G. Zappa, L. C. Shaffrey, K. I. Hodges, P. G. Sansom, and D. B. Stephenson. A multimodel assessment of future projections of north atlantic and european extratropical cyclones in the cmip5 climate models. *Journal of Climate*, 26(16):5846–5862, 2013b.

G. Zappa, M. K. Hawcroft, L. Shaffrey, E. Black, and D. J. Brayshaw. Extratropical cyclones and the projected decline of winter mediterranean precipitation in the cmip5 models. *Climate Dynamics*, 45(7):1727–1738, 2015.